RESEARCH ARTICLE SUMMARY

CANCER IMMUNOLOGY

Dendritic cells control tertiary lymphoid structure development and maintenance in cancer

Raphaël Mattiuz *et al.*

Full article and list of author affiliations: https://doi.org/10.1126/science.ady1678

INTRODUCTION: Lymphoid aggregates accumulate in chronic inflammatory lesions, including tumors. They consist of organized assemblies of innate and adaptive immune cells arising in nonlymphoid tissues and are thought to operate as local hubs for lymphocyte recruitment, (re)activation, and maintenance. The most mature aggregates, which develop T and B cell zones with germinal centers, are referred to as tertiary lymphoid structures (TLSs). The presence of TLSs is associated with superior prognosis and response to immune checkpoint blockade (ICB) in cancer, which makes these structures attractive therapeutic targets.

RATIONALE: Previous studies have identified DC-LAMP, expressed by mature dendritic cells (DCs), as a specific marker of human TLSs. Studies have also identified that CD11c$^+$ cells, which include DCs and other myeloid populations, are required for TLS persistence in mouse lung infection models. However, the precise contribution of major histocompatibility complex class I (MHC-I) and MHC-II antigen presentation, including cross-presentation by specific dendritic cell subsets, to TLS initiation, maintenance, and function in cancer remains unknown. Given the strong association of TLS presence with ICB response, defining the cellular and molecular drivers of TLSs in cancer is now a critical priority.

RESULTS: To address the role of DCs in TLS formation and maintenance, we developed a mouse model of non–small cell lung cancer (NSCLC) that forms mature TLSs (KP-HELLO-2) containing B cell follicles with germinal centers and T cell zones with T follicular helper (T_{FH}) cells and TCF1$^+$PD-1$^+$ progenitor exhausted CD8$^+$ T (T_{PEX}) cells. We show that, during early stages of tumor development, TLS formation relies on interferon-γ (IFN-γ)–driven maturation of type 1 conventional dendritic cells (cDC1s), migration of cDC1s to tumor-draining lymph nodes (tdLNs), WDFY4-dependent cross-presentation, and ultimately the recruitment of activated T cells to the tumor site.

As tumors progress, TLS maintenance becomes independent of T cell egress from tdLNs, coinciding with a significant reduction of cDC1 migration to tdLNs. Instead, mature cDC1s accumulate within intratumoral CCR7 ligand–enriched stromal hubs. Notably, timed depletion of cDC1s or preventing their migration to these stromal hubs after TLSs are formed disrupts TLS functional architecture and maintenance. We found that cDC1-mediated concomitant MHC-II and MHC-I antigen presentation to CD4$^+$ and CD8$^+$ T cells and intact CD40 signaling are critical for the maintenance of TLSs, the preservation of the T_{FH} cell pool, germinal center formation, tumor-specific immunoglobulin G (IgG) production, and the differentiation of T_{PEX} cells. Furthermore, expanding or activating DCs with FLT3L-Fc or CD40 agonist expands TLSs. Using spatial transcriptomics and multiplex imaging across various human tumors, we confirmed that mature DCs expressing high levels of CCR7 accumulate in TLSs close to CCL19$^+$ stromal hubs and interact with T_{FH} cells, T_{PEX} cells, and B cells. Moreover, the presence of mature DCs or TLSs correlates with improved overall survival in NSCLC and disease-free survival in hepatocellular carcinoma.

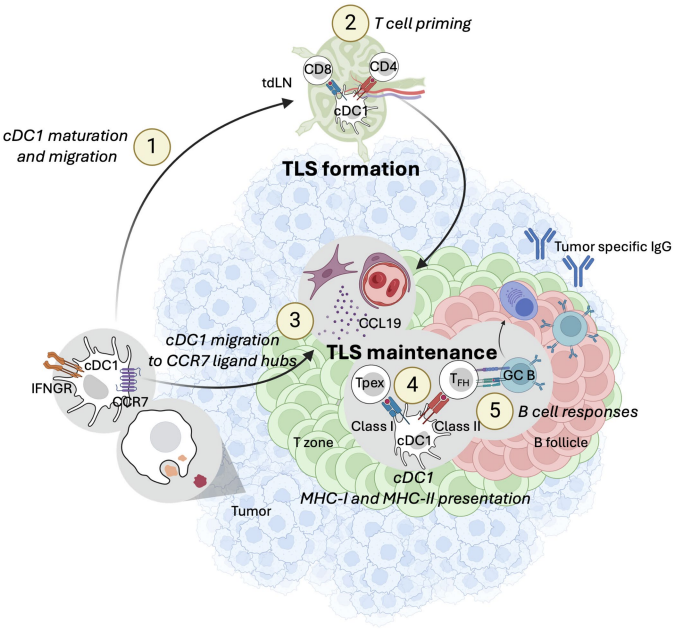

Mature cDC1s orchestrate TLS formation and maintenance through concomitant antigen presentation to CD4$^+$ and CD8$^+$ T cells. (1) TLS formation requires the maturation of cDC1s and their migration to tdLNs followed by (2) the recruitment of primed T cells into the tumor microenvironment. As tumors progress, (3) intratumoral migration of cDC1s into CCR7 ligand–enriched stromal hubs becomes essential for TLS maintenance. This process (4) depends on concomitant antigen presentation to both CD4$^+$ and CD8$^+$ T cells to sustain the T_{FH} cell pool, drive T_{PEX} cell differentiation, and (5) support germinal center (GC) formation and tumor-specific IgG production.

CONCLUSION: These findings underscore the pivotal role of mature cDC1s in both establishing and maintaining functional TLSs, primarily through concomitant MHC-II and MHC-I antigen presentation to CD4$^+$ and CD8$^+$ T cells within tumor lesions. They further highlight the therapeutic potential of cDC1-targeted strategies to enhance TLS function and improve antitumor immunity in cancer patients. □

Corresponding author: Miriam Merad (miriam.merad@mssm.edu) Cite this article as R. Mattiuz *et al.*, *Science* 393, eady1678 (2026). DOI: 10.1126/science.ady1678

CANCER IMMUNOLOGY

Dendritic cells control tertiary lymphoid structure development and maintenance in cancer

Raphaël Mattiuz[1,2], Jesse Boumelha[1,2]†, Emmanouil Aerakis[1,2,3]†, Jessica Le Berichel[1,2]†, Pauline Hamon[1,2]†, Laszlo Halasz[1,2], Abishek Vaidya[1,2,4], Brian Y. Soong[1,2], Emir Radkevich[1,2,5], Hye Mi Kim[6], Matthew D. Park[1,2], Romain Donne[1,2,7,8], Leanna Troncoso[1,2], Rachel A. Kaplan[1,2], Clotilde Hennequin[1,2], Isaias Hernández-Verdin[9], Lucía López[10], Frederika Rentzeperis[1,2], Darwin D'Souza[1,2,5], Medard Ernest Kaiza[6], Ian P. MacFawn[6,11], Meriem Belabed[1,2], Guillaume Mestrallet[1,2,8,12], Etienne Humblin[1,2], Raphaël Merand[1,2,5], Samarth Hegde[1,2], Jean-Christophe Lone[13], Giorgio Ioannou[1,2], Sinem Ozbey[1,2], Igor Figueiredo[1,2], Alexander Tepper[1,2,14], Hajer Merarda[1,2], Nadine Serhan[1,2], Maximilian M. Schaefer[1,2], Jinping An[15], Ray A. Ohara[16], Erika Nemeth[1,2], Simon Goldstein[1,2], Amanda M. Reid[1,2], Moataz Noureddine[4,17], Alexandra Tabachnikova[1,2], Giulia Maria Piperno[10], Maria Tsoumakidou[3], Jalal Ahmed[1,2], Alexandros D. Polydorides[18], Nina Bhardwaj[1,2,8,12], Amaia Lujambio[1,2,7,8], Zhihong Chen[1,2,5], Edgar Gonzalez Kozlova[1,2], Seunghee Kim-Schulze[1,2,5], Joshua D. Brody[1,2], Michael Schotsaert[1,2,13,17], Christine Moussion[19], Sacha Gnjatic[1,2], Vladimir Roudko[1,2,5], Florent Ginhoux[20], Kenneth M. Murphy[16], Catherine Sautès-Fridman[9], Wolf Herman Fridman[9], Brian D. Brown[1,2,14], Thomas U. Marron[1,2,12,21], Federica Benvenuti[10], Jason G. Cyster[15], Hélène Salmon[22], Tullia C. Bruno[6], Nikhil S. Joshi[23], Alice O. Kamphorst[1,2,8,24,25], Miriam Merad[1,2,5]*

Tertiary lymphoid structures (TLSs) are associated with immunotherapy response, yet the mechanisms controlling their formation and maintenance remain unclear. Using spatial transcriptomics and multiplex imaging across human tumors, we found that CCR7$^+$ mature dendritic cells (DCs) accumulate in TLSs. In a mouse non–small cell lung cancer model that forms mature TLSs, we show that early TLS development requires interferon-γ (IFN-γ)–driven type 1 conventional dendritic cell (cDC1) maturation, migration to tumor-draining lymph nodes (tdLNs), and T cell recruitment. As tumors progress, TLSs persist independently of tdLN T cell egress, coinciding with cDC1 accumulation within intratumoral CCL19 stromal hubs. There, cDC1–major histocompatibility complex class 1 (MHC-I) and –MHC-II concomitant antigen presentation, along with CD40 signaling, sustain TLS, T follicular helper (T_{FH}) cell pool, germinal centers, and tumor-specific immunoglobulin G (IgG). These findings highlight local mature cDC1s as key TLS orchestrators and potential targets to enhance antitumor TLS function.

Tertiary lymphoid structures (TLSs) are organized immune aggregates that resemble canonical secondary lymphoid organs, containing naïve and antigen-experienced T and B cells organized in T cell zones and B cell follicles, respectively (*1*, *2*). With few exceptions, patients with tumors enriched in TLSs have improved outcome and enhanced response to immune checkpoint blockade (ICB) (*3*–*7*), which suggests that TLSs may contribute to the priming of naïve T cells or enable the reactivation of effective T cell responses upon ICB treatment (*8*).

Previous findings have reported that TLSs in non–small cell lung cancer (NSCLC) are associated with DC-LAMP$^+$ mature dendritic cells (DCs) (*5*). However, the exact role for antigen presentation in the maintenance and functionality of TLSs remains unclear (*8*). Conventional dendritic cells (cDCs) are specifically equipped to prime and educate T cells (*9*). Two subsets of cDCs have been identified in humans and mice, including type 1 cDCs (cDC1s), which excel in the (cross-)presentation of cell-associated antigens to CD8$^+$ and CD4$^+$ T cells, and cDC2s, which are most potent to present soluble protein antigens to CD4$^+$ T cells (*9*, *10*). Both cDC1s and cDC2s up-regulate a similar gene expression program upon capture of antigens, becoming mature DCs that are specialized to modulate T cells (*11*). Using spatial transcriptomics and multiplex imaging analysis of various human tumors, we found that pathology-annotated TLSs are composed of cDCs in a mature molecular state along with T follicular helper (T_{FH}) cells, TCF1$^+$PD-1$^+$ progenitor exhausted CD8$^+$ T (T_{PEX}) cells, and B cells. Together, these results prompted us to explore the contribution of cDCs to the formation and maintenance of TLSs in tumor lesions.

Given that cDCs can both prime T cells within tumor-draining lymph nodes (tdLNs) and reactivate T cells at the tumor site, it became essential to develop models that allow for the conditional manipulation of cDCs to dissect their specific contributions in these distinct tissue sites. To address this, we engineered a tumor model that reliably forms mature TLSs and developed strategies for constitutive or conditional depletion or genetic manipulation of cDCs at different time points after tumor development. In this work, we show that mature DCs, particularly mature cDC1s, are central to TLS formation, maintenance, and function in tumors.

Results

Mature DCs are enriched in human TLSs, where they interact with T_{FH} cells and B cells across several tumor types

Mature DCs exhibit a discrete cellular program that is up-regulated in cDC1s and cDC2s upon capture of cell debris in tumor lesions and reflects the state in which cDCs interact with T cells (*11*, *12*). To map the spatial distribution of cDC subsets and states within human tumors, we performed spatial transcriptomics (Visium SD, 10x Genomics) analysis of human NSCLC, hepatocellular carcinoma (HCC), colorectal cancer (CRC), and clear cell renal cell cancer (ccRCC) (*13*). We found a substantial enrichment of mature DC (*CCR7*, *FSCN1*, *CD40*, *CD80*, *CCL17*, and *CCL22*), cDC1 (*XCR1*, *CLNK*, and *CADM1*), T_{FH} cell (*CXCL13*, *TCF7*, *ICOS*, *CD40LG*, and *PDCD1*), PD-1$^+$ CD8$^+$ T cell (*PDCD1*, *CD8A*, and *CD8B*), naïve T cell (*IL7R*, *CCR7*, and *TCF7*), memory B cell (*CD19* and *BANK1*), and germinal center B cell (*LMO2*, *MEF2B*, and *RGS13*) molecular programs in pathology-annotated intratumoral TLSs but de-enrichment at the tumor core (Fig. 1A and fig. S1, A to C; https://rstudio-connect.hpc.mssm.edu/mattiuz_science2026_tls_spatial_data/). By contrast, monocyte and macrophage gene programs were distributed both within and outside TLSs (fig. S1B). We also examined gene expression pathways associated with mature DCs, either by characterizing those found in mature DC-rich TLS spots from spatially mapped human tumor lesions (fig. S1D) or mature DCs identified in TLS-enriched NSCLC and HCC lesions by single-cell RNA sequencing (scRNA-seq) (*14*, *15*) (table S1). In both analyses, we found that mature DCs in TLS-enriched lesions up-regulated major histocompatibility complex class 2 (MHC-II) and MHC-I antigen presentation machinery and CD40 signaling pathways (fig. S1, E and F).

To investigate mature DC cellular interactions within TLSs at the single-cell level in NSCLC and HCC, we used a targeted spatial transcriptomic technology (MERFISH) to map 500 gene probes that we had previously identified to be highly enriched in tumor lesions by scRNA-seq (*14*–*16*) (table S2). We confirmed that mature DCs were significantly enriched in TLSs within the tumor compared with their immature counterparts (cDC1s and cDC2s) (Fig. 1B and fig. S1G). Notably, tumor cDC1s displayed higher expression of mature DC-associated genes compared with cDC2s (fig. S1H). Because DC maturation is linked to the uptake of cellular debris (*11*, *12*), this suggests a greater accumulation of tumor antigen–loaded cDC1s within TLSs.

Proximity analysis revealed that within TLSs, mature DCs were closely located (within a 30-μm radius) to naïve B and T cells, germinal center B cells, and T_{FH} and T_{PEX} cells (Fig. 1C and fig. S1, G, I, and J). DC-LAMP, encoded by *LAMP3*, was found to be exclusively expressed by mature DCs within the immune compartment of NSCLC and HCC by scRNA-seq (fig. S1K). Using multiplex imaging, we confirmed at the protein level that DC-LAMP$^+$ mature DCs and CLEC9A$^+$ cDC1s were enriched in TLSs (Fig. 1D, fig. S1L, and table S3). Furthermore, we identified an intermediate state along the cDC1–to–mature DC transition, enriched in TLSs, which coexpresses CLEC9A and DC-LAMP (fig. S1M). We also found that mature DCs were primarily located in the T cell zone or at the T-B zone border close to high endothelial venules (HEVs), similar to their positioning in lymph nodes (*17*) (Fig. 1E and fig. S1, N and O), and there was a similar density of mature DCs in TLSs with or without germinal centers (fig. S1P).

In patients with locally advanced or metastatic NSCLC who failed platinum therapy, a randomized phase 2 trial (POPLAR) comparing PD-L1 blockade (atezolizumab) with chemotherapy (docetaxel) reported a significant survival benefit of PD-L1 blockade over chemotherapy (*18*). Bulk RNA-seq analysis of pretreatment biopsies within this cohort showed that those with higher TLS density, as annotated by a pathologist, exhibited a robust mature DC gene signature and superior survival outcomes (Fig. 1F and fig. S2A). Furthermore, in these patients, the mature DC signature correlated with signatures of components of TLSs, including T_{FH} cells, T_{PEX} cells, and naïve B and T cells (fig. S2B and table S4). These observations strongly suggest that enrichment in mature DCs correlates with TLS occurrence and can serve as a prognostic marker for improved survival (*5*). We confirmed the signature correlations in pretreatment biopsies from the BIONIKK trial, which included 199 metastatic kidney cancer patients treated with anti–PD-1 (nivolumab), anti–PD-1, and anti-CTLA4 (nivolumab and ipilimumab) or VEGFR tyrosine kinase inhibitors (*19*) (fig. S2C). Furthermore, in a cohort of HCC patients treated with neo-adjuvant anti–PD-1 (cemiplimab) (*20*), patients enriched in TLSs in posttreatment tumor resections had improved disease-free survival, which was associated with increased tumor infiltration of mature DCs and local T cell clonal expansion (Fig. 1G and fig. S2, D and E). Collectively, these findings underscore the potential key role of mature DCs within TLSs in fostering the response to ICB in human tumors, which prompted our interest in understanding the contribution of mature DCs in TLS formation, maintenance, and function in tumors.

Mature cDC1s accumulate within TLSs in preclinical lung cancer tumors

To study the role of cDCs in the formation and function of TLSs in cancer, we used a modified mouse lung adenocarcinoma (LUAD) line, named KP-HELLO-2, derived from *KRAS$^{LSL\text{-}G12D}$;Trp53$^{fl/fl}$* (KP) mice (*21*) expressing the model antigen HELLO (neoantigen fusion of the B cell antigen HEL, the CD8 epitope GP33, and the CD4 epitope GP66) (*22*) and the Thy-1.1 antigen (CD90.1) (Fig. 2A). Intravenous injection of KP-HELLO-2 cells led to the formation of orthotopic lung adenocarcinoma lesions with high numbers of intratumoral TLSs with defined T cell and B cell zones (Fig. 2B; fig. S3, A to C; and movies S1 and S2), many of which displayed prominent germinal centers that harbored CD21$^+$ stromal follicular dendritic cells (FDCs) adjacent to activation-induced cytidine deaminase (AID)$^+$ germinal center B cells (Fig. 2C). Consistent with what we observed in human tumor lesions, mouse TLSs were enriched in germinal center B cells (B220$^+$BCL6$^+$), T_{FH} cells (CD4$^+$PD-1$^+$TCF1$^+$/BCL6$^+$), and T_{PEX} cells (CD8$^+$TCF1$^+$PD-1$^+$) located in close proximity (Fig. 2D, fig. S3D, and table S5) as well as tumor antigen–specific pretransferred CD4$^+$ T cells (CD4$^+$CD45.1-SMARTA$^+$) and endogenous B cells (B220$^+$HEL$^+$) (Fig. 2E). Furthermore, DCs expressing high levels of CCR7, MHC-II, and CD86 accumulated in TLSs, where they interacted with CD4$^+$ T cells, CD8$^+$ T cells, and B cells (Fig. 2F).

TLSs were inversely correlated with tumor burden, which suggests that these structures contributed to antitumor immunity (Fig. 2G). Imaging analysis of tumor lesions in *Xcr1^{mCherry}* cDC1-reporter mice confirmed that cDC1s (CD11c$^+$*Xcr1-mCherry*$^+$) accumulated in TLSs in proximity to T and B cells (Fig. 2H), as observed in human cancer lesions, and most cDC1s charged with tumor antigens (mScarlet$^+$) were in a mature state (CD40$^+$CD86$^+$) (Fig. 2I and fig. S3E). We confirmed by multiplex immunofluorescence that mature cDC1s (F4/80$^-$CD11b$^-$CD11c$^+$CD86$^+$) were enriched in TLSs (Fig. 2J), where they exhibited more cell-cell interactions compared with outside TLSs, particularly with cell types most enriched within TLSs, including T_{FH} cells, T_{PEX} cells, and germinal center B cells (fig. S3F). We confirmed using *Ms4a3^{Cre};Rosa26$^{lox\text{–}stop\text{–}lox\text{-}Tdt}$* mice and inducible *Ms4a3^{CreERT2}; Rosa26$^{lox\text{–}stop\text{–}lox\text{-}Tdt}$* mice, which constitutively or conditionally trace monocyte-derived cells (*23*, *24*), that cDCs accumulating in TLSs were bona fide, lineage-committed cDC1s and cDC2s, rather than monocyte-derived DCs (fig. S3, G and H).

To probe whether cDCs or specific cDC subsets played a role in TLS formation, we injected KP-HELLO-2 cells into *Xcr1-DTA* mice that specifically lacked cDC1s (fig. S3I). We generated these mice by crossing *Xcr1^{Cre}* mice (*25*) with *Rosa26$^{lox\text{–}stop\text{–}lox\text{-}DTA}$* mice to enable constitutive depletion of XCR1$^+$ cDC1s while sparing cDC2s (*26*, *27*). Absence of cDC1s led to significantly reduced TLSs in both number and size and reduced T_{FH} cells (CXCR5$^+$PD-1$^+$ CD4$^+$ T cells), interferon-γ (IFN-γ$^+$) CD4$^+$ T cells, CD8$^+$ T cells, and germinal center B cells within tumors, which was accompanied by increased tumor burden (Fig. 2K and table S6). Similar results were obtained upon injection of KP-HELLO-2 cells into cDC1-deficient *Batf3$^{-/-}$* mice (fig. S3, I and J). cDC1 depletion also had a major effect on the functional architecture of remaining lymphoid aggregates which were devoid of germinal center B cells, T_{FH} cells, and T_{PEX} cells (fig. S3K). Moreover, using *Wdfy4$^{-/-}$* mice, deficient in cDC1-mediated cross-presentation (*28*), we observed a significant reduction in TLS numbers and a decrease in PD-1$^+$ CD8$^+$ T cells (fig. S3L), indicating impaired induction of tumor-specific CD8$^+$ T cells. Given the role of cDC1 cross-presentation and their close interaction with both CD8$^+$ and CD4$^+$ T cells, we interrogated whether T cells were also required for TLS formation. Depletion of either CD4$^+$ or CD8$^+$ T cells resulted in a significant reduction in TLS numbers (fig. S3M).

cDC1s were also required for intratumoral TLS formation in autochthonous lung adenocarcinomas in KP genetically engineered mouse model (GEMM), in mice challenged with orthotopic Hep-53.4 liver

[1]Marc and Jennifer Lipschultz Precision Immunology Institute, Icahn School of Medicine at Mount Sinai, New York, NY, USA. [2]Department of Immunology and Immunotherapy, Icahn School of Medicine at Mount Sinai, New York, NY, USA. [3]Institute for Bioinnovation, "Alexander Fleming" Biomedical Sciences Research Center, Vari, Greece. [4]Graduate School of Biomedical Sciences, Icahn School of Medicine at Mount Sinai, New York, NY, USA. [5]Human Immune Monitoring Center, Icahn School of Medicine at Mount Sinai, New York, NY, USA. [6]Tumor Microenvironment Center, Department of Immunology, UPMC Hillman Cancer Center, University of Pittsburgh, Pittsburgh, PA, USA. [7]Liver Cancer Program, Division of Liver Diseases, Department of Medicine, Icahn School of Medicine at Mount Sinai, New York, NY, USA. [8]Tisch Cancer Center, Icahn School of Medicine at Mount Sinai, New York, NY, USA. [9]Department of Immunology, Inflammation, Complement and Cancer, Centre de Recherche des Cordeliers, Sorbonne Université, INSERM, Université Paris Cité, Paris, France. [10]Cellular Immunology, International Centre for Genetic Engineering and Biotechnology, ICGEB, Trieste, Italy. [11]Department of Biology, Grove City College, Grove City, PA, USA. [12]Division of Hematology and Medical Oncology, Icahn School of Medicine at Mount Sinai, New York, NY, USA. [13]GIMM, Gulbenkian Institute for Molecular Medicine and Faculdade de Medicina da Universidade de Lisboa, Lisbon, Portugal. [14]Icahn Genomics Institute, Icahn School of Medicine at Mount Sinai, New York, NY, USA. [15]Howard Hughes Medical Institute and Department of Microbiology and Immunology, University of California, San Francisco, San Francisco, CA, USA. [16]Department of Pathology and Immunology, Washington University in St. Louis School of Medicine, St. Louis, MO, USA. [17]Global Health and Emerging Pathogens Institute and Department of Microbiology, Icahn School of Medicine at Mount Sinai, New York, NY, USA. [18]Henry D. Janowitz Division of Gastroenterology, Department of Medicine, and Department of Pathology, Molecular and Cell-Based Medicine, Icahn School of Medicine at Mount Sinai, New York, NY, USA. [19]Genentech, South San Francisco, CA, USA. [20]Paris-Saclay University, Gustave Roussy, INSERM U1015, Villejuif, France. [21]Institute for Thoracic Oncology, Icahn School of Medicine at Mount Sinai, New York, NY, USA. [22]Institut Curie, Paris, France. [23]Department of Immunobiology, Yale University School of Medicine, New Haven, CT, USA. [24]Department of Oncological Sciences, Icahn School of Medicine at Mount Sinai, New York, NY, USA. [25]Department of Graduate Education, Icahn School of Medicine at Mount Sinai, New York, NY, USA. ***Corresponding author. Email: miriam.merad@mssm.edu** †These authors contributed equally to this work.

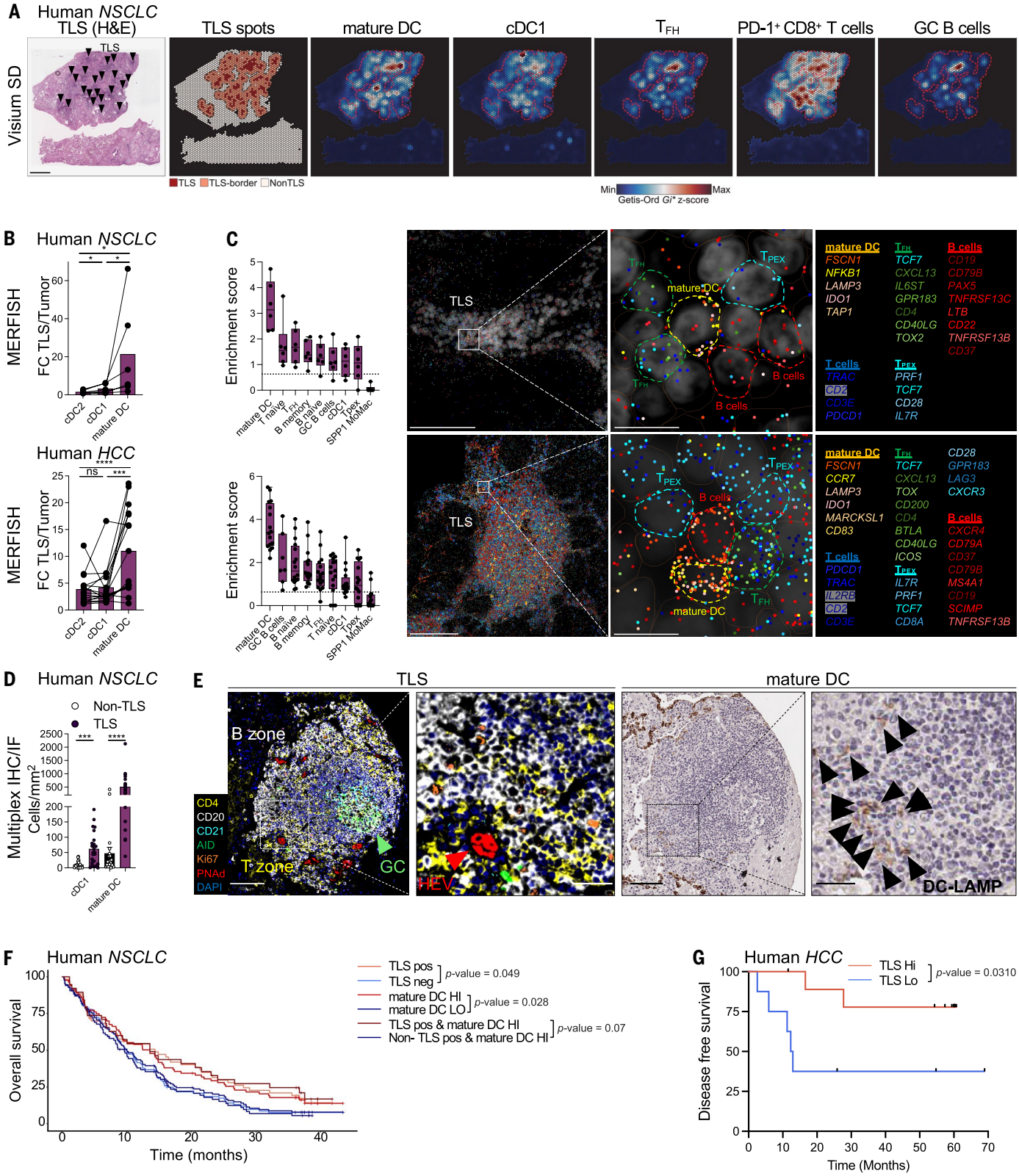

Fig. 1. Mature DCs accumulate in TLSs across human cancers. (**A**) FFPE Visium SD spatial transcriptomics analysis of NSCLC tumors ($n = 2$ patients). Representative Visium SD slide showing pathology-annotated TLS (left; scale bar, 1 mm); TLS and border spots (two layers of spots located outside the TLS); and hotspots for mature DC, cDC1, T_{FH} cell, PD-1^+ $CD8^+$ T cell, and germinal center (GC) B cell gene signatures inferred from scRNA-seq references (right). (**B** and **C**) MERFISH spatial transcriptomics analysis of NSCLC ($n = 6$ patients and slides) and HCC ($n = 14$ patients and 16 slides) tumors. In HCC, GC B cells were identified only in MERSCOPE panel 2 ($n = 7$ patients and slides). (B) Fold change of mature DC, cDC1, and cDC2 populations in TLS versus non-TLS areas in NSCLC (top) and HCC (bottom). $^*P < 0.05$; $^{***}P < 0.001$; $^{****}P < 0.0001$ (Wilcoxon rank sum test); bars indicate the mean. (C) Cell proximity analysis showing enrichment score for immune populations within 30 μm of mature DCs in TLS areas; box-and-whisker

plots showing the median (center line), interquartile range (box), and minimum-to-maximum whiskers, with representative TLS area illustrating interactions between mature DCs, T_{FH} cells, T_{PEX} cells, and B cells in NSCLC [top; scale bars, 100 μm (left) and 10 μm (right)] and HCC [bottom; scale bars, 200 μm (left) and 10 μm (right)]. (**D**) Quantification of mature DC (DC-LAMP$^+$) and cDC1 (CLEC9A$^+$) densities in non-TLS versus TLS regions by multiplex IHC (MICSSS) in NSCLC patients ($n = 23$ patients); epithelial cells expressing DC-LAMP were excluded from the analysis. ***$P < 0.001$; ****$P < 0.0001$ (paired t test); data indicate means ± SEMs. (**E**) Representative multiplex immunofluorescence (IF) staining of a mature TLS (CD4, CD20, CD21, AID, Ki67, PNAd, DAPI), paired with consecutive DC-LAMP IHC staining of NSCLC tumors. Representative of 14 mature TLSs (tissue microarray from a cohort of 41 patients). Scale bars, 100 μm (overview) and 50 μm (zoom). (**F**) Bulk transcriptomes paired with TLS annotations in NSCLC ($n = 168$ patients, including 60 TLS^{HI} patients, from Genentech POPLAR dataset). Kaplan-Meier analysis compares overall survival of TLS-positive versus TLS-negative patients, mature DC-high versus mature DC-low patients, and TLS-positive/mature DC-high patients versus all other patients. Statistics by log-rank (Mantel-Cox) test. (**G**) Kaplan-Meier analysis comparing disease-free survival of TLS-high versus TLS-low HCC patients ($n = 18$ patients) treated with neoadjuvant PD-1 blockade [$P = 0.0310$, log-rank (Mantel-Cox) test].

tumors, and for peritumoral TLS formation in mice with orthotopic AKPS colon tumors (fig. S3, N and O). Notably, mature cDC1s generated in vitro upon capture of apoptotic KP-HELLO-2 tumor cells were also sufficient to drive the formation of immune aggregates ex vivo upon coculture with purified intratumoral T and B cells within tumor spheroids (fig. S3P).

CCR7 and IFN-γ receptor expression on cDCs is critical for TLS formation

We next sought to investigate the cDC molecular signals that regulate TLS formation in tumors. Using the Visium SD spatial transcriptomics platform to quantify gene signature scores in mature DC–enriched TLS spots, we observed an enrichment in IFN-γ gene signature (fig. S3Q). IFN-γ receptor (IFN-γR) signaling promotes cDC immunogenic function and their ability to instruct effective antitumor T cell responses (*11*, *26*, *29*). To examine whether IFN-γ signaling in cDCs plays a role in TLS formation, we generated mice lacking IFN-γR specifically within the cDC compartment (*Zbtb46*^{Cre}*;Ifngr1*$^{fl/fl}$ mice) (Fig. 2L). We found that absence of IFN-γR signaling prevented cDC maturation (CD40$^+$), reduced TLS formation, and increased tumor burden, which was accompanied by a marked decrease in T_{FH} cells, IFN-γ$^+$ CD4$^+$ T cells, and CD8$^+$ T cells within tumors (Fig. 2L). This prompted us to identify the source of IFN-γ locally and in tdLNs. We found that IFN-γ is primarily produced by PD-1$^+$ CD8$^+$ T cells and ICOS$^+$ CD4$^+$ T cells in tumor-bearing lungs and T helper 1 (T_H1)–like (CXCR6$^+$) and T_{FH}-like (PD-1$^+$ICOS$^+$) cells in tdLNs (fig. S3R). Furthermore, multiplex immunofluorescence revealed that IFN-γ was primarily secreted in TLSs by T_{FH} cells and, to a lesser extent, T_{PEX} cells (fig. S3S).

CCR7 up-regulation is required for cDC migration to the T zone of secondary lymphoid organs toward CCR7 ligands produced by the lymphatic endothelium and stromal cells that populate the T zone (*30*, *31*), which helps position cDCs charged with tissue antigens in proximity to naïve T cells, thus enabling the priming of tumor-specific immunity. To probe whether cDC migration to secondary (or tertiary) lymphoid organs through CCR7 ligands contributed to TLS formation, we generated mice lacking *Ccr7* specifically within the cDC compartment (*Zbtb46*^{Cre}*;Ccr7*$^{fl/fl}$ mice) (Fig. 2M) and challenged these mice with KP-HELLO-2 tumors. CCR7 deletion in cDCs significantly disrupted TLS development and increased tumor burden with a notable decrease in T_{FH} cells, IFN-γ$^+$ CD4$^+$ T cells, CD8$^+$ T cells, and germinal center B cells in tumors (Fig. 2M). Altogether, these results establish that IFN-γ–driven maturation and CCR7-dependent cDC migration to lymphoid structures contribute to the formation of TLSs in lung cancer lesions.

cDC1s are required locally for TLS maintenance

cDCs are required for T cell priming in tdLNs, and efficient priming of T cells may contribute to the formation of TLSs, but cDCs also interact with T cells within tumor tissues and may contribute to TLS maintenance locally. To examine whether TLS formation is dependent on cDCs within tdLNs or at the tumor site, we first explored the contribution of T cells primed in tdLNs to TLS formation using FTY720 to inhibit lymphoid egress from the tdLNs (*32*). We found that inhibition of T cell egress during the first 9 days after tumor engraftment significantly reduced TLS formation, whereas inhibition of T cell egress after day 9 had little effect on the number of TLSs in tumors (Fig. 3A). These results establish that T cell priming in the tdLNs is critical for TLS formation but not for TLS maintenance locally in tumor lesions, which prompted us to measure longitudinal changes in immune cell composition that were associated with TLS formation and maintenance in tumors.

Longitudinal profiling of tumor lesions revealed that intratumoral immature TLSs arise from or near the vasculature and progress toward mature TLSs with the formation of B cell follicles and T cell zones at later time points (Fig. 3B). Specifically, we observed a marked increase in TLS number and size during tumor progression, and the increase in TLSs was particularly steep after day 8 (Fig. 3B). Notably, the number of mature cDC1s and cDC2s carrying tumor-associated antigens (mScarlet$^+$) increased in the tdLNs until day 8 after tumor implantation, after which their accumulation in the tdLNs was strongly reduced while they instead started to accumulate locally at the tumor site (Fig. 3C). Tumor-specific CD4$^+$, T_{FH} cell, and T_H1 cell populations were maintained over time (Fig. 3D), whereas there was a steady accumulation of antigen-experienced (PD-1$^+$) and terminally exhausted (CD39$^+$TCF1$^-$PD-1$^+$) CD8$^+$ T cells during tumor progression (Fig. 3E). At later time points, coinciding with the greatest expansion of TLSs, we also observed a substantial expansion of T_{PEX} cells (CD39$^-$TCF1$^+$PD-1$^+$) (Fig. 3E) accompanied by a significant increase in the frequency of germinal center B cells and class-switched tumor-specific immunoglobulin G (IgG) antibodies (Fig. 3F). Altogether, these observations reveal that the accumulation of mature cDC1s and cDC2s in tumors correlates with the accumulation of T_{PEX} cells, germinal center B cells, IgG antibody production, and TLS expansion at the tumor site, which prompted us to explore the role of tumor-infiltrating cDCs in TLS maintenance locally.

To probe the role of cDCs in TLS maintenance, we generated two models to either deplete the entire cDC compartment or specifically cDC1s starting at day 8 after tumor implantation to allow for T cell priming, egress from the tdLNs, and accumulation in tumor tissues. We reconstituted wild-type (WT) mice with bone marrow cells isolated from mice expressing the diphtheria toxin receptor (DTR) within ZBTB46$^+$ cDC (*Zbtb46-DTR*), which enables restricted cDC depletion after DT injection while sparing endothelial cells, which also express *Zbtb46* (*33*) (fig. S4A). We also generated *Xcr1-DTR* mice by crossing *Xcr1*^{Cre} mice with *Rosa26*$^{lox-stop-lox-DTR}$ mice to enable timed deletion of XCR1$^+$ cDC1s and mature cDC1s that have expressed *Xcr1* while sparing cDC2s (*25*–*27*) (fig. S4A). We found that the depletion of the entire cDC compartment, or specifically the cDC1 subset, at day 8 after tumor engraftment significantly reduced TLS numbers in tumor tissues at similar levels (Fig. 3G), so we subsequently focused on the role of cDC1s in TLS maintenance in tumor-bearing mice.

cDC1 depletion reduced the frequency of T_{FH} cells in tumors (Fig. 3H), led to a disappearance of germinal centers (Fig. 3I), reduced the number of CD8$^+$ T cells and proliferating cells within TLSs, and reduced the number of AID$^+$ Ki67$^+$ germinal center B cells (Fig. 3J) and tumor-specific IgM and class-switched IgG antibodies (Fig. 3K and fig. S4B). Altogether, these results established that cDC1s are required locally for the maintenance and function of TLSs.

To further confirm that cDC1s promote TLS maintenance through local interaction with tumor-infiltrating T cells, we blocked late-stage tdLN egress after priming occurred. We found that whereas blocking

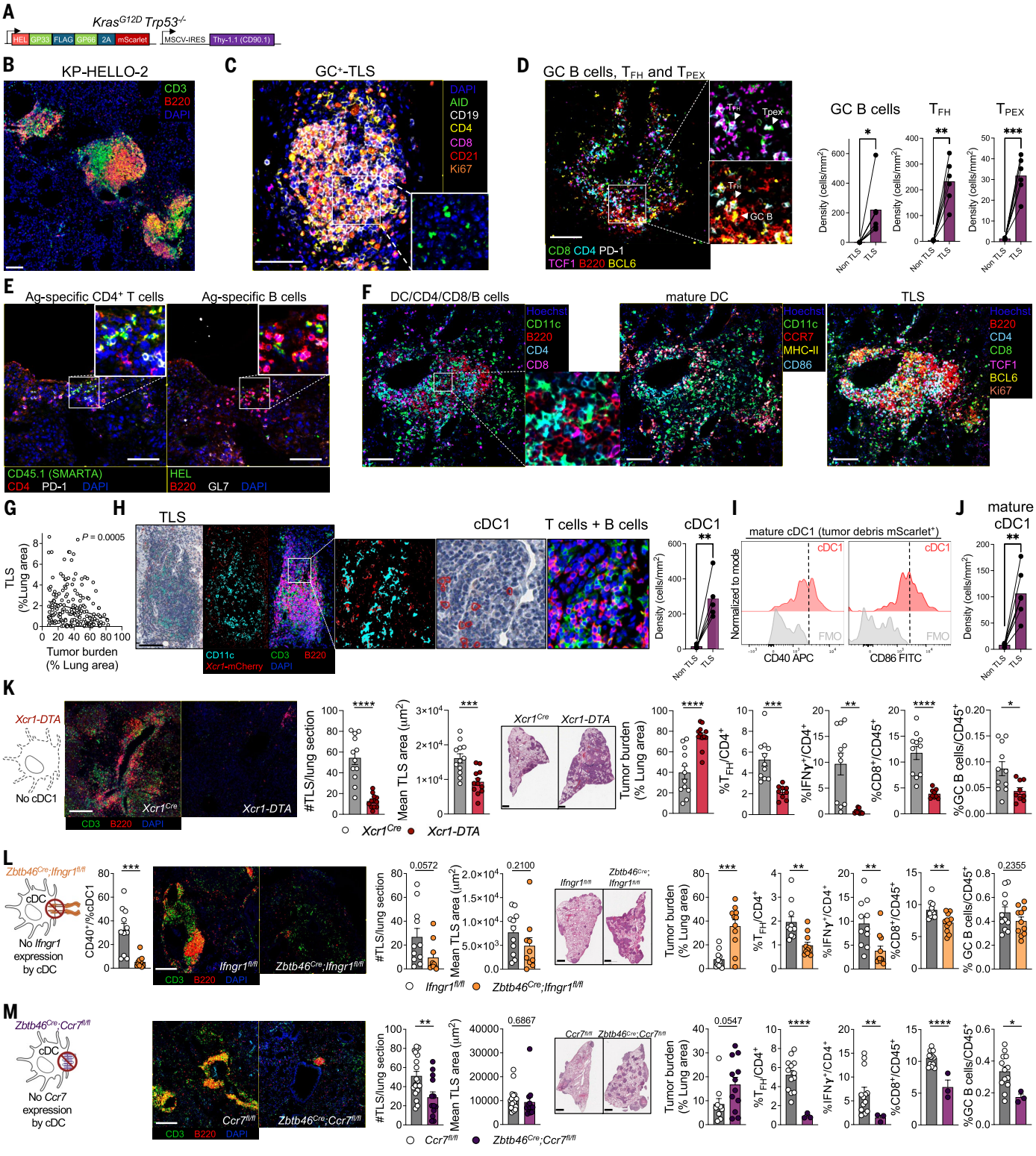

Fig. 2. Mature cDC1s control TLS formation. (**A**) Schematic representation of constructs used to generate KP-HELLO-2. (B to H and J) Immunofluorescence analysis of representative KP-HELLO-2 TLS at day 15 postengraftment in WT mice. (**B**) Staining of B cell and T cell zones with B220 and CD3. Scale bar, 100 µm. (**C**) GC$^+$-TLS stained with AID, CD19, CD4, CD8, CD21, and Ki67. Representative of 7 mice. Scale bar, 50 µm. (**D**) Representative images (CyCIF) and density quantification of GC B cells (B220$^+$ BCL6$^+$), T_{FH} cells (CD4$^+$ PD-1$^+$ TCF1$^+$/BCL6$^+$), and T_{PEX} cells (CD8$^+$ PD-1$^+$ TCF1$^+$) in TLS and non-TLS areas (TLS identified by CD4, CD8, PD-1, B220, and DAPI staining). $n = 6$ mice. Scale bar, 100 µm. *$P < 0.05$; **$P < 0.01$; ***$P < 0.001$ (paired t test); bars indicate the means. (**E**) Adoptively transferred antigen-specific CD4 T cells (SMARTA CD45.1) stained with CD45.1, PD-1, and CD4; endogenous antigen-specific B cells stained with HEL antigen, B220, and GL7. Representative of 10 mice. Scale bar, 100 µm. (**F**) Mature DCs (CD11c$^+$ MHC-II$^+$ CCR7$^+$ CD86$^+$) within mature TLSs stained with B220, CD4, CD8, TCF1, BCL6, and Ki67. Representative of 8 mice (CyCIF). Scale bar, 100 µm. (**G**) Immunofluorescence analysis of TLS (stained for CD3, B220, and DAPI) and tumor area assessed by H&E on consecutive sections at day 15 postengraftment. Inverse correlation between TLS area and tumor area (percentage of lung area) in WT mice ($n = 196$, pooled from 27 independent experiments). Linear regression analysis, $P = 0.0005$. (**H**) Representative images of

TLS from *Xcr1-mCherry-Cre* mice showing CD3 and B220 immunofluorescence, paired with consecutive IHC staining for CD11c and mCherry, and quantification of cDC1 density in TLS and non-TLS areas ($n = 5$ mice). Scale bar, 100 μm. $^{**}P < 0.01$ (paired *t* test); bars indicate the means. (**I**) cDC1 maturation status (CD40 and CD86 expression in mScarlet$^+$ cDC1s) at day 12 postengraftment (representative of 13 mice from two independent experiments). (**J**) Density quantification (CyCIF) of mature cDC1s (F4/80$^-$ CD11b$^-$ CD11c$^+$ CD86$^+$) in TLS and non-TLS areas (identified by CD4, CD8, PD-1, B220, and DAPI staining). $n = 6$ mice. $^{**}P < 0.01$ (paired *t* test); bars indicate the means. (**K** to **M**) Immunofluorescence of TLS (CD3, B220, and DAPI; scale bar, 200 μm) number and mean size, tumor area assessed by H&E on consecutive sections (scale bar, 1 mm) and tumor-bearing lung quantification of T_{FH} cells (PD-1$^+$ CXCR5$^+$ CD4$^+$), GC B cells (CD19$^+$ IgD$^-$ IgM$^-$ GL7$^+$), IFN-γ$^+$ CD4$^+$, and CD8$^+$ T cells by flow cytometry on day 15 in *Xcr1-DTA* ($n = 12$ per group, representative of two independent experiments; data indicate means ± SEMs) (K), *Zbtb46^{Cre}; Ifngr1$^{fl/fl}$* ($n = 10$ to 11 per group, representative of two independent experiments; data indicate means ± SEMs) with flow cytometry quantification of CD40 expression on cDC1s in tumor-bearing lungs on day 15 (L), and *Zbtb46^{Cre}; Ccr7$^{fl/fl}$* mice ($n = 13$ to 20 per group, pooled from two independent experiments; data indicate means ± SEMs) (M) versus littermate controls. $^{*}P < 0.05$; $^{**}P < 0.01$; $^{***}P < 0.001$; $^{****}P < 0.0001$ (unpaired *t* test).

T cell egress at day 8 after tumor implantation did not affect TLS number, concomitant cDC1 depletion at day 9 significantly reduced TLS maintenance in tumors (Fig. 3L). Accordingly, we found that administration of the DC growth factor FMS-like tyrosine kinase 3 ligand agonist fused to an Fc domain (FLT3L-Fc) on day 8 after tumor implantation significantly increased the number of cDCs and cDC1s (fig. S4C) and doubled TLS numbers in tumors (Fig. 3M). Additionally, administration of FLT3L in mice after implantation of parental KP-HELLO tumor cells, which do not form mature TLSs, tended to increase TLS formation (fig. S4D). Also, in metastatic breast cancer patients, we observed increased TLS formation in one out of six patients after FLT3L treatment as compared with their pretreatment biopsy (fig. S4E). Collectively, these results indicate that TLS maintenance and function in tumor tissues depended on tumor-infiltrating mature cDC1s, and therapeutic strategies boosting intratumoral DCs can promote TLS formation. In line with the role of TLSs in antitumor immunity and the requirement of cDC1s for TLS maintenance, depletion of cDC1s at day 8 after tumor implantation significantly reduced overall survival of tumor-bearing mice (Fig. 3N).

cDC1 migration to CCR7 ligand–enriched stromal hubs locally control TLS maintenance

The observation that cDCs significantly altered their migration trajectory to accumulate in tumor tissues rather than in the tdLNs after day 8 post–tumor engraftment suggested that they were actively recruited to a tissue hub. To explore the molecular signals that promoted cDC migration to specific tumor sites and their contribution to TLS maintenance locally, we generated a ligand-receptor analysis map across the different cellular compartments that populate TLSs in human NSCLC lesions using MERFISH (Fig. 4A). We found that mature DCs within TLSs expressed the highest levels of ligand-receptor pairs that interact with CD4$^+$ T cells, including PD-L1 (*CD274*), PD-L2 (*PDCD1LG2*), *ICOSLG*, *CD80*/*86*, CCR4 ligands (*CCL17* and *CCL22*), and *CD40*. Mature DCs expressed high *CCR7* levels, whereas we have previously shown that one of the CCR7 ligands, namely *CCL19*, was highly expressed by ADH1B$^+$ cancer-associated fibroblasts (CAFs) and perivascular cells (*16*). We subsequently validated the spatial proximity of ligand-receptor pairs using Visium HD (fig. S5A). Accordingly, spatial transcriptomic analysis of NSCLC revealed that *CCL19*-expressing perivascular cells and ADH1B$^+$ CAFs were enriched in proximity to mature DCs within TLSs (fig. S5, B to E). We confirmed the close interaction within TLSs between CCL19-expressing cells, stromal cells, mature DCs, and T cells at single-cell resolution using Visium HD on three NSCLC patients (fig. S5F). Using multiplex imaging analysis, we confirmed that in human NSCLC, TLSs were enriched in CCL19-producing ADHB1$^+$ CAFs and MYH11$^+$ perivascular cells located in proximity to mature DCs (Fig. 4B). Similarly in mouse tumors, TLSs were enriched in CCL19, and cDCs accumulated in CCL19$^+$ regions within TLSs (Fig. 4C). Because CCR7 is the main receptor for CCL19, we examined whether deletion of CCR7 in cDC1s after T cells are primed and recruited to tumor sites compromises TLS maintenance in tumor tissues. To enable the temporal deletion of CCR7 specifically in the cDC1 subset, we reconstituted CD45.1$^+$ mice with 1:1 (*Xcr1-DTR* CD45.2$^+$:*Ccr7*$^{-/-}$ CD45.1$^+$/CD45.2$^+$) mixed bone marrow cells (Fig. 4D). DT administration at day 8 after tumor engraftment resulted in the depletion of the entire CCR7-proficient WT cDC1 compartment, whereas the remaining cDC1s lacked CCR7 (fig. S6A). Notably, CCR7 deletion from cDC1s at day 8 after tumor implantation significantly reduced the number and size of TLSs and reduced the number of T_{FH} cells in lung tumors (Fig. 4E).

Similar findings were obtained upon CCR7 deletion from the whole cDC compartment using mice reconstituted with 1:1 (*Zbtb46-DTR* CD45.2$^+$:*Ccr7*$^{-/-}$ CD45.1$^+$/CD45.2$^+$) mixed bone marrow (fig. S6, A and B). Temporal deletion of CCR7 from cDC1s prevented their accumulation in TLSs and altered the functional architecture of remaining lymphoid aggregates, which contained reduced germinal center B cells, T_{FH} cells, T_{PEX} cells, and naïve T cells (fig. S6, C and D). Furthermore, CCR7 deficiency reduced cellular interactions of mature cDC1s (fig. S6E) and prevented their migration toward CCL19-expressing cells (fig. S6F). Mature DCs also express *CCL19* (Fig. 4A and fig. S5A); however, conditional deletion of CCL19 from cDC1s did not alter TLS maintenance in tumors (Fig. 4F) and did not affect the accumulation of CCR7$^+$ cDC1s and T cells in tumor-bearing lungs (fig. S6G). These data strongly suggest that cDC1 migration to CCR7 ligand–enriched stromal hubs are required for TLS maintenance in tumor lesions.

cDC1s orchestrate TLS maintenance through local concomitant antigen presentation to CD4$^+$ and CD8$^+$ T cells

A major role of mature cDC1s is to present tissue-associated antigens to T cells. Within the DC compartment, cDC1s are known to excel in the (cross-)presentation of cell-associated antigens to both CD4$^+$ and CD8$^+$ T cells in secondary lymphoid organs (*34*, *35*). cDC1s have also been shown to provide a key scaffold to recruit CD4$^+$ and CD8$^+$ T cells, enabling CD4$^+$ T cells to provide helper cytokines in the vicinity of CD8$^+$ T cells, which promotes their differentiation into CD8$^+$ effector T cells in a process that requires CD40 signaling in cDC1s (*25*, *34*, *35*). To investigate whether CD40 licensing of cDC1s by CD4$^+$ T cells was required for TLS maintenance in tumors, we reconstituted mice with 1:1 (*Xcr1-DTR*:*Cd40*$^{-/-}$) mixed bone marrow cells to enable temporal depletion of CD40$^+$ cDC1s upon DT administration, sparing the remaining cDC1s lacking CD40. DT administration 8 days after tumor implantation reduced TLS number and size as well as the number of CD8$^+$ T cells (fig. S7A).

To assess whether cDC1 sustained antigen presentation to CD4$^+$ T cells was required to maintain TLSs locally, we reconstituted mice with mixed bone marrow cells from *Xcr1-DTR* and MHC-II knockout (MHC-II–KO) mice and treated them with DT at day 8 postimplantation. Notably, MHC-II deletion from cDC1s 8 days after tumor implantation (fig. S7B) significantly reduced the number and size of TLSs, resulting in the dispersion of T cells and B cells within the tissue (Fig. 5A). This also reduced the number of T_{FH} cells, CD8$^+$ T cells, and PD-1$^+$ CD8$^+$ T cells; increased the relative frequency of T_{PEX} cells within this compartment; and reduced tumor-binding IgG antibodies (Fig. 5, B and C, and fig. S7C). Using the same strategy, we also abrogated MHC-I cross-presentation of tumor antigens through conditional deletion of *B2m* from cDC1s. Deletion of MHC-I$^+$ cDC1s 8 days after tumor implantation (fig. S7B) significantly reduced the number and size of TLSs, albeit to a lesser extent than deletion of MHC-II$^+$ cDC1s (Fig. 5A). Disruption of

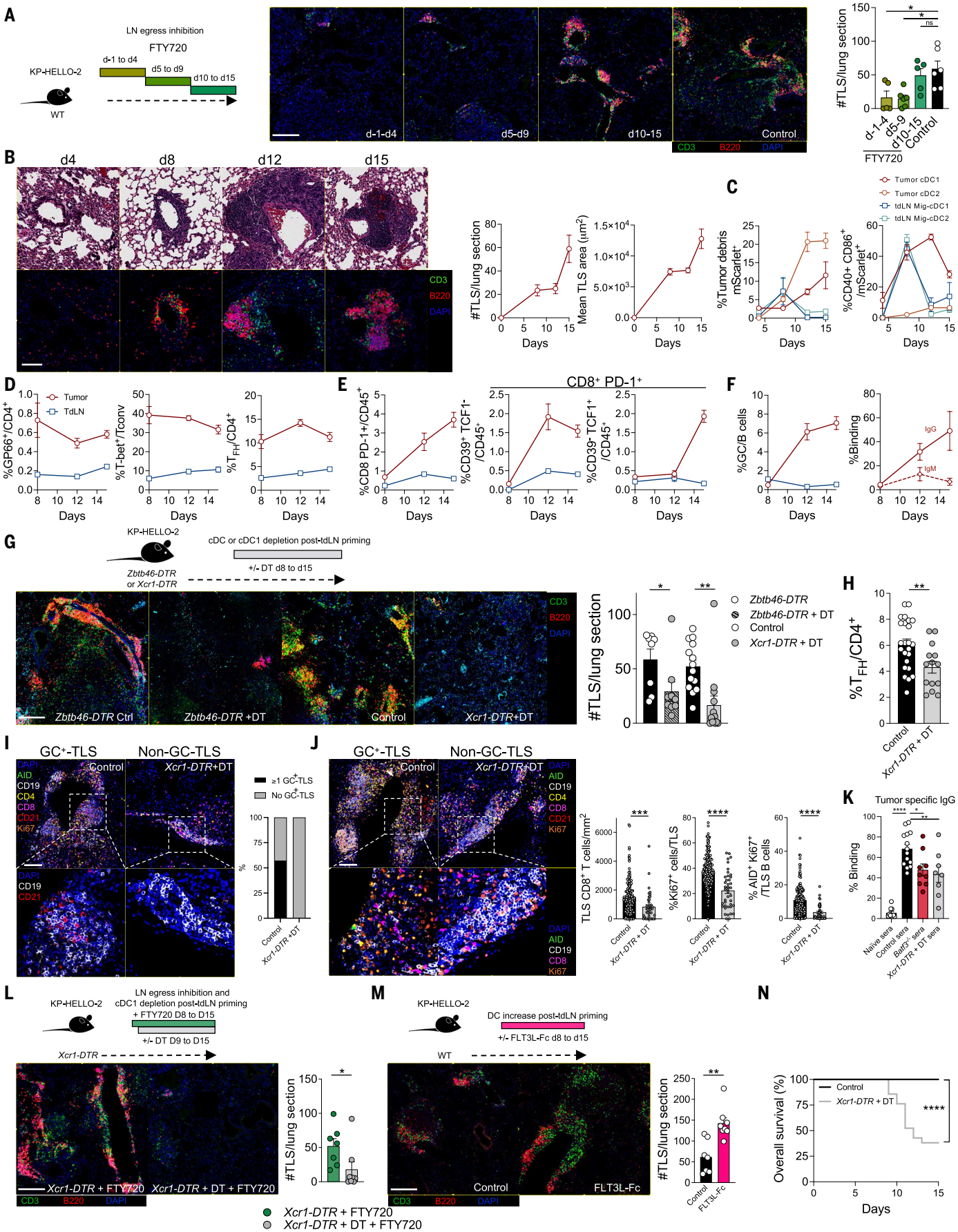

Fig. 3. Mature cDC1s are required locally for TLS maintenance and function. (A to C, G, I, J, L, and M) Immunofluorescence analysis of TLS (CD3, B220, and DAPI staining) and quantification at day 15 or as indicated. (**A**) T cell egress from tdLNs blocked with FTY720 from day 1 to day 4, day 5 to day 9, or day 10 to day 15 after tumor engraftment. TLS quantification was performed at day 15 ($n = 5$ to 6 per group, representative of two independent experiments; data indicate means ± SEMs). Scale bar, 200 μm. (**B** to **F**) TLS formation kinetics ($n = 6$ to 7 per time point, representative of two independent experiments; data indicate means ± SEMs), with H&E staining on consecutive sections showing vessels (scale bar, 100 μm) (left), TLS number, and mean size (right) (B), and kinetic analysis of immune populations in tumor and tdLNs by flow cytometry, including percentages of DC uptaking tumor debris (mScarlet$^+$) (left) and their maturation (CD40$^+$ CD86$^+$) (right) (C). (D) Tumor antigen–specific, T-bet$^+$, and T_{FH} (PD-1$^+$ CXCR5$^+$) cells among CD4$^+$ T cells. (E) CD8$^+$ PD-1$^+$ T cells, subdivided into CD39$^+$ TCF1$^-$ and CD39$^-$ TCF1$^+$ populations, among immune cells. (F) GC B cells among B cells (left) and kinetics of serum IgG and IgM binding to tumor cells ex vivo at the indicated time points (right). (G to K) DC or cDC1 depletion using DT from day 8 to day 15 in DTR mice. (**G**) TLS quantification in *Zbtb46-DTR*, *Xcr1-DTR*, and control mice treated or not with DT ($n = 8$ to 14 per group, pooled from two independent experiments; data indicate means ± SEMs). Scale bar, 200 μm. (**H**) Quantification of tumor-bearing lung T_{FH} cells among CD4$^+$ T cells at day 15 in *Xcr1-DTR* mice treated with DT versus control mice ($n = 14$ to 25 per group, pooled from four independent experiments; data indicate means ± SEMs). (**I** and **J**) GC$^+$-TLS staining (AID, CD19, CD4, CD8, CD21, and Ki67) in *Xcr1-DTR* mice treated with DT versus control mice, with zoom depicting follicular DCs (CD19$^-$ CD21$^+$) within GC$^+$-TLS and proportions of mice with ≥1 GC$^+$-TLS ($n = 3$ to 7 per group, 196 TLS analyzed, including 7 GC$^+$-TLS) per whole lung slide (I). Scale bar, 100 μm. (J) AID, Ki67, and CD8 staining within TLS and quantification of CD8$^+$ T cells, Ki67$^+$ cells, and AID$^+$ Ki67$^+$ B cells in TLS of *Xcr1-DTR* mice treated with DT versus control mice ($n = 3$ per group, 229 TLS analyzed; data indicate means ± SEMs). Scale bar, 100 μm. GC B cells coexpressing AID (green) and Ki67 (orange) appear in yellow. (**K**) Serum IgG binding to tumor cells ex vivo from naïve, control, *Batf3*$^{-/-}$, and *Xcr1-DTR* treated with DT mice ($n = 8$ to 14 per group, pooled from two independent experiments; data indicate means ± SEMs). Sera were collected at day 15. (**L**) TLS quantification in *Xcr1-DTR* mice treated with FTY720 starting at day 8 with or without DT starting at day 9 ($n = 6$ to 8 per group; data indicate means ± SEMs). Scale bar, 200 μm. (**M**) TLS quantification in WT mice treated or not with FLT3L-Fc at day 8 ($n = 7$ to 8 per group, representative of two independent experiments; data indicate means ± SEMs). Scale bar, 200 μm. [(A), (G), (H), and (J) to (M)] *$P < 0.05$; **$P < 0.01$; ***$P < 0.001$; ****$P < 0.0001$ (unpaired *t* test). (**N**) Overall survival of *Xcr1-DTR* mice treated with DT (from day 8 to day 15) versus control mice ($n = 21$ to 29 per group, pooled from three independent experiments), with all mice reaching the humane end point by day 15 postengraftment. ****$P < 0.0001$ [log-rank (Mantel-Cox) test].

MHC-I cross-presentation did not affect the proportion of T_{FH} cells (Fig. 5B) or tumor-binding IgG antibodies (Fig. 5C). However, similar to the results observed upon MHC-II deletion from cDC1s, abrogating MHC-I antigen presentation from cDC1s reduced the relative number of CD8$^+$ T cells and antigen-experienced PD-1$^+$ CD8$^+$ T cells and increased the relative frequency of T_{PEX} cells within this compartment (Fig. 5B and fig. S7C). In line with a role of cDC1 antigen presentation to CD4$^+$ T cells as a requirement for TLS maintenance, CD40 agonism has been shown to expand intratumor TLSs in patients and mice (*36*). To interrogate whether this effect of CD40 agonism is dependent on MHC-II presentation, we treated tumor-bearing control mice or *Xcr1-DTR*:MHC-II–KO that received DT with CD40 agonist (Fig. 5D). In contrast to control mice, CD40 agonism was unable to expand TLSs when MHC-II presentation was abrogated on cDC1s, highlighting an essential role for MHC-II antigen presentation for TLS expansion. To determine whether cDC1 coexpression of MHC-I and MHC-II is required for local TLS maintenance, we reconstituted mice with mixed bone marrow—50% from *Xcr1-DTR* mice, 25% from MHC-II–KO mice, and 25% from *B2m*$^{-/-}$ mice—and administered DT on day 8 after tumor implantation (Fig. 5E). To ensure that 25% WT bone marrow was sufficient to generate functional cDC1s capable of maintaining TLSs, we reconstituted mice with 75% *Xcr1-DTR* and 25% WT bone marrow and observed no significant reduction in TLS numbers after DT administration (fig. S7D). Critically, selective depletion of MHC-I$^+$ MHC-II$^+$ cDC1s (fig. S7B) significantly reduced TLS numbers and size, which indicates that concomitant antigen presentation to both CD8$^+$ and CD4$^+$ T cells by cDC1s is essential to sustain TLSs locally (Fig. 5F and fig. S7D). We were unable to measure the effect on the tumor burden because these tumors progress fast and were quite advanced when we administrated DT.

Conditional deletion of interleukin-12 (IL-12) or IFN-γR from cDC1s did not alter TLS maintenance (fig. S7, E and F), which suggests that intact IFN-γR signaling in cDC1s is critical for efficient priming of T cells in the tdLNs and the formation of TLSs but is dispensable for the maintenance of TLSs in tumors. In line with these results, mature DCs within TLSs in human NSCLC and HCC tumor lesions showed a down-regulation of interferon-stimulated genes (ISGs) compared with cDC1s (fig. S7G), suggesting that IFN-γR signaling does not control DC–T cell interactions in TLSs once DCs mature. Taken together, our results reveal that in situ cDC1 migration to stromal hubs producing CCR7 ligands and sustained concomitant presentation of tumor antigens to CD4$^+$ and CD8$^+$ T cells at the tumor site control the quantity and quality of TLSs and enable the maintenance of T_{FH} cells, the production of tumor-specific IgG antibodies, and the differentiation of T_{PEX} cells.

Discussion

By leveraging spatial transcriptomics and multiplex imaging analysis of various human tumors and a mouse model of NSCLC that forms mature TLSs, we identified a critical role for the DC subset, cDC1s, in the formation, maintenance, and function of TLSs. We show that within the first week after tumor implantation, TLS formation relied on IFN-γ–driven maturation of cDC1s, their migration to the tdLNs, and the subsequent recruitment of activated T cells to the tumor site. As tumors progressed, TLS maintenance became independent of tdLN T cell egress and instead depended on cDC1 migration to CCR7 ligand–enriched stromal hubs, sustained antigen presentation to intratumoral CD4$^+$ and CD8$^+$ T cells, and CD40 signaling. These interactions were crucial for the maintenance of the T_{FH} cell pool, the formation of germinal centers, and the production of tumor-specific antibodies, collectively sustaining TLS functionality and adaptive immune responses within the tumor microenvironment.

These results extend previous research indicating that DCs present antigens to tumor-specific T cells within tumor-associated TLSs (*37*) and that DCs control TLS maintenance in homeostatic conditions in the gut (*38*) and in virally infected lungs (*39*, *40*). Our findings are in line with the recent observation that neoadjuvant intratumoral poly-ICLC, a DC activator, induces TLSs and clinical response in prostate cancer (*41*).

cDC1s ability to present antigens to both CD4$^+$ and CD8$^+$ T cells and to be licensed by CD4$^+$ T cells through CD40 signaling for cross-priming of CD8$^+$ T cells in tdLNs has been shown to be required for optimal antitumor immunity (*25*) and antiviral immune response (*34*, *35*). By depleting cDC1s at a stage when TLSs are no longer reliant on T cell recruitment from the tdLNs, we demonstrate that local cDC1-mediated concomitant antigen presentation to intratumoral CD4$^+$ and CD8$^+$ T cells, along with CD40 signaling, is essential for maintaining TLS structure and functionality. We confirmed that CD40 agonism expands TLSs (*36*) and further show that this expansion critically depends on cDC1 antigen presentation. Therapies aimed at boosting intratumoral DC abundance and promoting their activation represent an optimal strategy to promote TLS response.

Much like in lymph nodes, DCs within TLSs are strategically positioned in the T cell zone or at the interface between the T and B zones. We found that T_{FH} cells are present in TLSs before germinal center formation, whereas depletion of cDC1s significantly reduced germinal center B cells in TLSs, suggesting that interactions between mature DCs and T_{FH} cells contribute to the germinal center response. Additionally, similar to chronic viral infection where cDC1s preserve T_{PEX} cells through MHC-I–dependent interactions within splenic niches (*42*), we

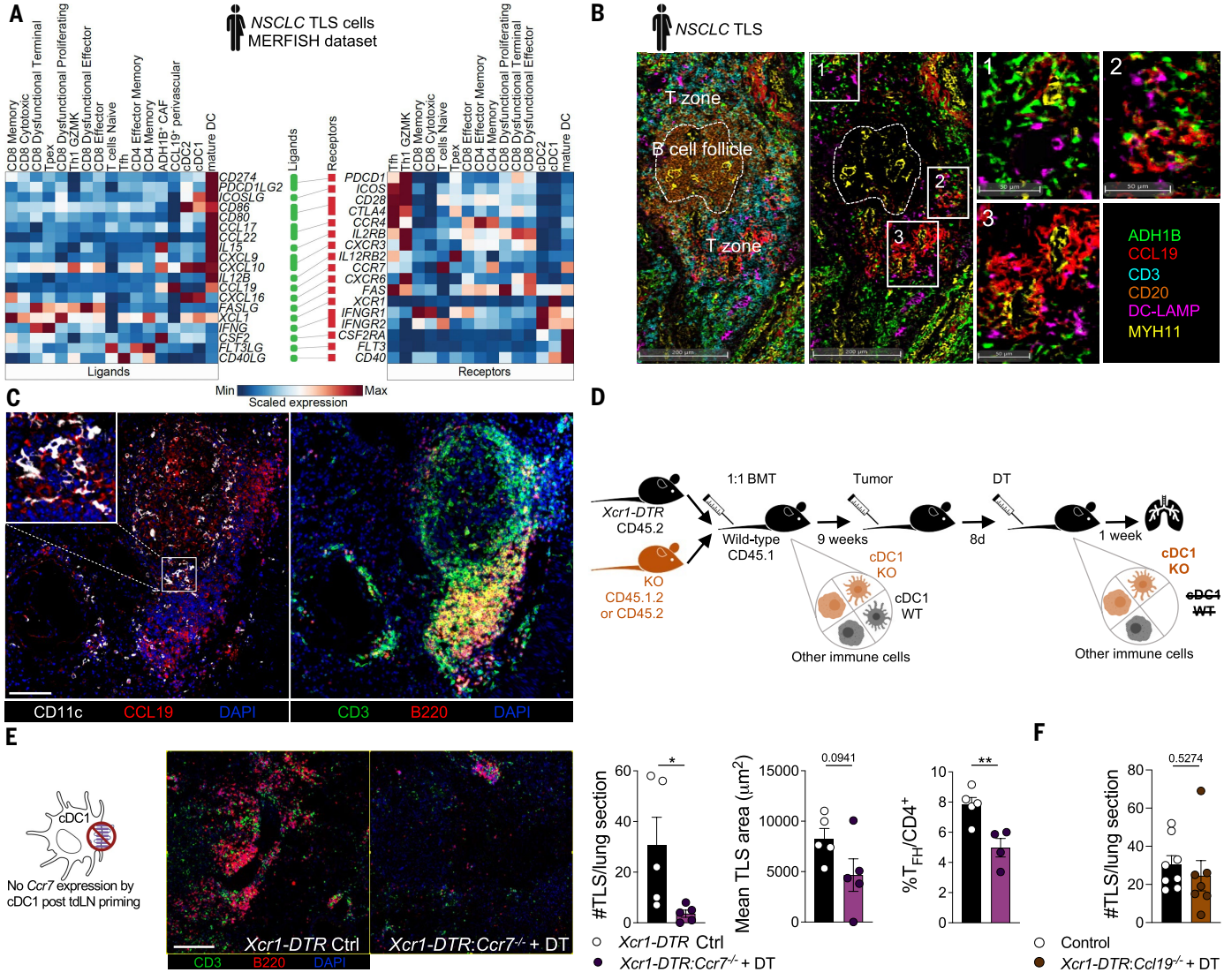

Fig. 4. Local cDC1 migration to CCR7 ligand hubs controls TLS maintenance. (**A**) Heatmap showing relative expression of ligand-receptor pairs by MERFISH between ADH1B$^+$ CAF, CCL19 perivascular cells, DCs, and T cell populations within TLSs in NSCLC patients ($n = 6$ patients). (**B**) Representative multiplex IHC staining of a TLS from an NSCLC tumor (stained for ADH1B, CCL19, CD3, CD20, DC-LAMP, and MYH11), representative of three patients. Panel 1 shows CCL19 with both ADH1B$^+$ and MYH11$^+$ cells, panel 2 shows CCL19 colocalizing with ADH1B$^+$ cells, and panel 3 shows CCL19 around MYH11$^+$ cells. Scale bars, 200 μm (overview) and 50 μm (zoom). (**C**) TLS from WT mice at day 15 postengraftment showing CD11c, CCL19, and DAPI immunofluorescence, paired with consecutive staining for CD3, B220, and DAPI. Representative of four mice. Scale bar, 100 μm. (**D**) Schematic of *Xcr1-DTR*: KO 1:1 mixed bone marrow chimeras experiments; DT administration starting at day 8 after tumor engraftment resulted in the depletion of the entire WT cDC1 compartment, leaving only cDC1s that are KO for the genes of interest. (**E** and **F**) Immunofluorescence analysis of TLS (stained for CD3, B220, and DAPI) with quantification of TLS number and mean area at day 15. (E) Comparison of *Xcr1-DTR* controls versus DT-treated *Xcr1-DTR:Ccr7*$^{-/-}$ CD45.1.2 mice ($n = 5$ per group, representative of two independent experiments; data indicate means ± SEMs). Scale bar, 200 μm. Tumor-bearing lung quantification of T_{FH} cells among CD4$^+$ T cells by flow cytometry at day 15. (F) Comparison of control bone marrow chimera versus DT-treated *Xcr1-DTR:Ccl19*$^{-/-}$ mice ($n = 7$ to 8 per group; data indicate means ± SEMs). $^*P < 0.05$; $^{**}P < 0.01$ (unpaired *t* test).

found that depletion of MHC-II and MHC-I from cDC1s promoted the accumulation of T_{PEX} cells, which suggests that cDC1s within tumor-associated TLSs contribute to T_{PEX} cell differentiation into effector CD8$^+$ T cells through direct MHC-I interaction and by offering proximal CD4$^+$ help through MHC-II antigen presentation. This physical interaction may promote T_{FH} cell help to T_{PEX} cells, including through IL-21 as previously suggested (*15*, *22*). Supporting this, our findings demonstrate that cDC1s engage in cognate interactions with both CD4$^+$ and CD8$^+$ T cells simultaneously within the TLSs rather than in distinct spatiotemporal niches. Consistent with this view, recent work has demonstrated that cDC1s interact simultaneously with CD4$^+$ and CD8$^+$ T cells in tumors after immunotherapy (*43*). The importance of MHC-II presentation in antitumor immunity corroborates evidence that ICB response relies on both MHC-I and MHC-II presentation of tumor neoantigens in preclinical tumor models (*44*) and that the DC ability to present antigens to both CD4$^+$ and CD8$^+$ T cells is required for efficient tumor response to adoptive T cell therapy (*45*). Furthermore, clonal expansion of T_{FH} cells and effector CD8$^+$ T cells strongly correlate with ICB response in patients with HCC (*15*). Similarly, our finding that alteration of TLS maintenance affect tumor antibody formation reinforces the importance of TLSs in the production of tumor-specific antibodies (*13*).

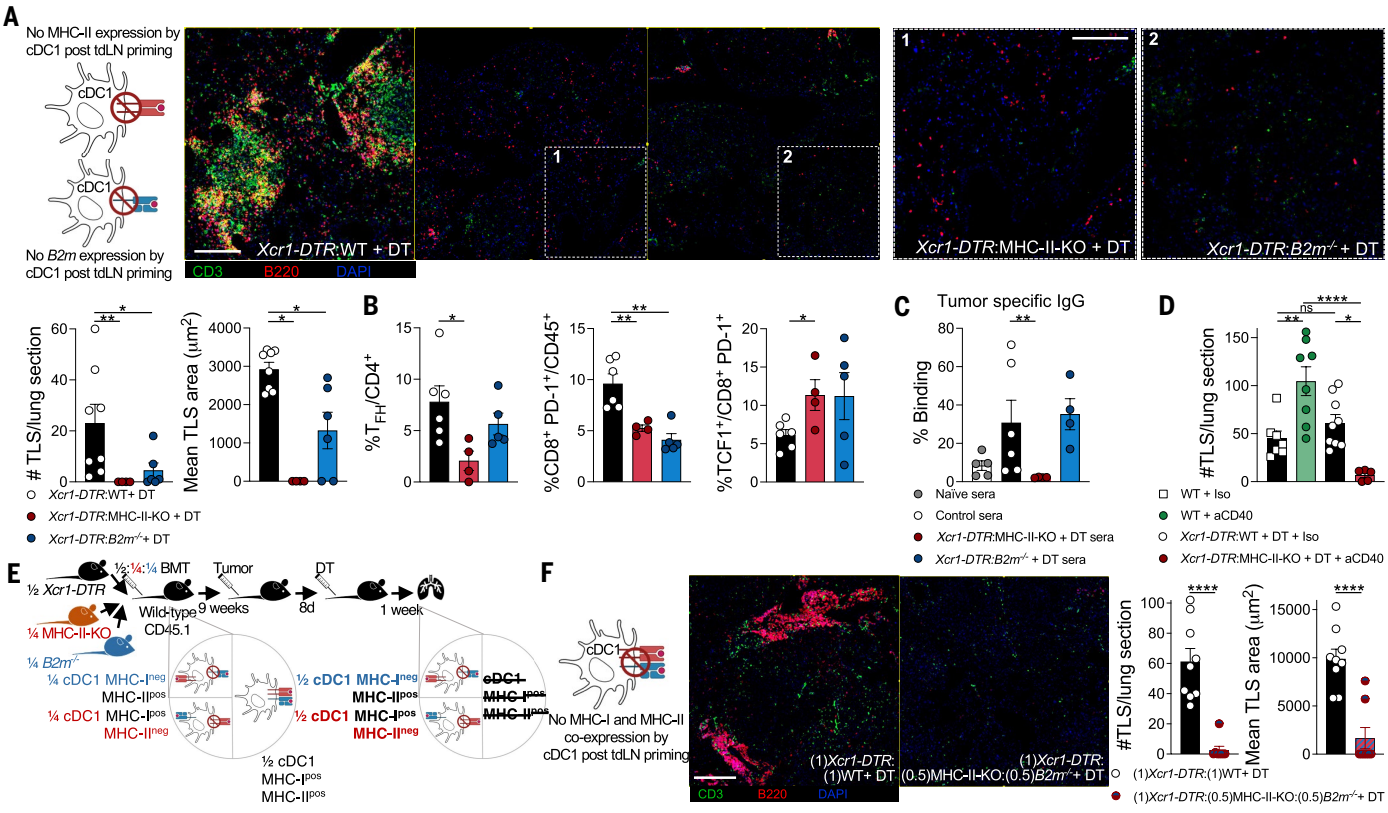

Fig. 5. Local cDC1 concomitant MHC-I and MHC-II antigen presentation controls TLS maintenance. (A, D, and F) Immunofluorescence analysis of TLS (stained for CD3, B220, and DAPI) with quantification of TLS number at day 15. (**A** and **B**) Comparison of DT-treated *Xcr1-DTR*:WT versus *Xcr1-DTR*:MHC-II–KO and *Xcr1-DTR:B2m*$^{-/-}$ mice ($n = 4$ to 8 per group, representative of two independent experiments; data indicate means ± SEMs). (A) Panels 1 and 2 depict B cell and T cell dispersion (right). Scale bars, 200 µm (overview) and 100 µm (zoom). TLS number and mean area are from day 15. (B) Tumor-bearing lung quantification by flow cytometry at day 15 includes T_{FH} cells among CD4$^+$ T cells, CD8$^+$ PD-1$^+$ T cells among immune cells, and TCF1$^+$ cells among CD8$^+$ PD-1$^+$ T cells. (**C**) Serum IgG binding to tumor cells ex vivo from naïve, *Xcr1-DTR*:WT, *Xcr1-DTR*:MHC-II–KO, and *Xcr1-DTR:B2m*$^{-/-}$ treated with DT mice ($n = 4$ to 6 per group, representative of two independent experiments; data indicate means ± SEMs). Sera were collected at day 15. (**D**) Comparison of WT treated with isotype control or anti-CD40 and DT-treated *Xcr1-DTR*:WT treated with isotype control versus *Xcr1-DTR*:MHC-II–KO treated with anti-CD40 ($n = 5$ to 9 per group; data indicate means ± SEMs). (**E**) Schematic of (1)*Xcr1-DTR*:(0.5)MHC-II–KO:(0.5)*B2m*$^{-/-}$ mixed bone marrow chimeras experiments; DT administration starting at day 8 after tumor engraftment resulted in the depletion of the entire WT MHC-I^{pos} MHC-II^{pos} cDC1 compartment, leaving only cDC1 that are MHC-I^{neg} MHC-II^{pos} or MHC-I^{pos} MHC-II^{neg}. (**F**) Comparison of DT-treated (1)*Xcr1-DTR*:(1)WT chimeras versus (1)*Xcr1-DTR*:(0.5)MHC-II–KO:(0.5)*B2m*$^{-/-}$ chimeras ($n = 8$ to 9 per group, representative of two independent experiments; data indicate means ± SEMs). TLS number and mean area are from day 15. [(A) and (C)] *$P < 0.05$; **$P < 0.01$ (Mann-Whitney *U* test). [(B) and (F)] *$P < 0.05$; **$P < 0.01$; ****$P < 0.0001$ (unpaired *t* test). (D) *$P < 0.05$; **$P < 0.01$; ****$P < 0.0001$ (one-way ANOVA followed by Tukey's multiple comparisons test).

Conditional targeting of DC function after priming did not significantly alter tumor burden at end point, even though TLS maintenance was compromised. This could be due to the rapid progression of the tumor model, which may not allow enough time to observe a more pronounced effect. Using less aggressive GEMMs may be better suited to studying the effect of TLS function on tumor progression.

We observed that TLS-associated DCs exhibit a distinct mature molecular state, referred to as "mregDC" (*11*). The mregDC program is driven by tumor debris uptake and cholesterol mobilization (*12*) and leads to expression of CCR7, enabling the migration of mature DCs to CCR7 ligand–enriched sites and efficient T cell priming. The enrichment of mature DCs in TLSs suggests that antigen capture is a prerequisite for their migration and accumulation. We further identified CCL19-producing fibroblasts and perivascular cells as potential pivotal TLS organizers forming chemokine-rich hubs that guide the recruitment and interaction of CCR7$^+$ mature DCs, T cells, and B cells (*46*). The positioning of CCR7$^+$ DCs in CCL19$^+$ perivascular niches may also contribute to antitumor immunity (*47*) and could precede the development of mature TLSs. Future lineage-tracing and time-stamping studies will examine the fate of cDC1s in tdLNs compared with TLSs, including their migration and half-life. Notably, fibroblast reticular cells producing CCL19 were recently shown to promote T cell aggregates, including TLSs, in NSCLC (*48*) and CRC liver metastasis (*49*). Chronic microbial exposure in the lungs promotes CCL19 in stromal cells and drives the formation of TLSs in the lung (*50*), and similar CCL19 hubs have been observed in chronic inflammatory psoriasis skin lesions (*51*). These observations emphasize the potential key role of CCL19 in the formation of TLSs, although the distinct contributions of CCL19 and the other CCR7 ligand CCL21 to TLS maintenance in tumors remain to be addressed. Like many chemokine receptors, CCR7 can be desensitized or down-regulated after prolonged exposure to its ligands. This phenomenon may reconcile our observations with previous findings showing that MHC-II$^+$ CCR7$^-$ cDC1s were able to cross-present antigen to CD8$^+$ T cells (*52*). In addition to stromal hubs, DCs and T_{FH} cells are also likely key organizers of TLSs (*15*, *53*). Mature DCs produce CCL17 and CCL22, two chemokine ligands known to recruit CCR4$^+$ CD4$^+$ T cells (*11*, *54*), whereas T_{FH} cells express high levels of cholesterol 25-hydroxylase (*CH25H*), an enzyme that generates oxysterol gradients known to recruit Ebi2$^+$ cells (*55*), which include both DCs and T_{PEX} cells (*15*). Furthermore, cDC1s specifically express XCR1 chemokine receptor, whereas its ligand, XCL1, is produced by T_{PEX} cells (*56*). The exact contribution of these molecules to TLS dynamics remains to be examined.

Our study identifies cDC1s and their sustained antigen presentation to both CD4$^+$ and CD8$^+$ T cells as a pivotal driver of TLS formation

and maintenance within tumors, emphasizing the importance of cDC1s in coordinating TLS functionality. The interplay between TLSs and tdLNs in mediating tumor-specific immunity likely shifts throughout tumor progression, with TLSs emerging as key contributors in more advanced tumors. In this setting, TLSs may provide essential hubs to support the survival of antigen-experienced lymphocytes and to amplify the efficiency of adaptive immune responses against tumor antigens. Our findings provide a potential foundation for therapeutic strategies aimed at enhancing effective antitumor T cell and B cell responses in cancer patients.

Materials and methods

TLS spatial data

An interactive website for exploring TLS spatial data (Visium SD/HD, MERFISH, and CyCIF) is available at https://rstudio-connect.hpc.mssm.edu/mattiuz_science2026_tls_spatial_data/.

Mouse strains

C57BL/6, B6.Cg-*Zbtb46*$^{tm3.1(cre)Mnz}$/J (strain no. 028538), B6.129P2(C)-*Ccr7*^{tm1Rfor}/J (no. 006621), C57BL/6N-*Ifngr1*$^{tm1.1Rds}$/J (no. 025394), B6.129S(C)-*Batf3*^{tm1Kmm}/J (no. 013755), C57BL/6-*Gt(ROSA)26Sor*$^{tm1(HBEGF)Awai}$/J (no. 007900), B6.129P2-*Gt(ROSA)26Sor*$^{tm1(DTA)Lky}$/J Strain (no. 009669), B6.Cg-*Gt(ROSA)26Sor*$^{tm14(CAG-tdTomato)Hze}$/J (no. 007914), B6(129S4)-*Xcr1*$^{tm1.1(cre)Kmm}$/J (no. 035435), SMARTA (H2-I-Ab-restricted LCMV GP61-80 epitope, B6.Cg-*Ptprc*^{a} *Pepc*^{b} Tg(TcrLCMV)1Aox/PpmJ) CD45.1 (no. 030450) mice were purchased from JAX, *Ccr7* floxed mice were donated by M. Bogunovic and I. Aifantis and C57BL/6J-*Ms4a3*$^{em2(cre)Fgnx}$/J (no. 036382) and *Ms4a3*^{CreERT2} were donated by F. Ginhoux. For bone marrow transplant experiments, CD45.1, B6.129P2-*Cd40*^{tm1Kik}/J (strain no. 002928), B6.129P2-*B2m*^{tm1Unc}/DcrJ (no. 002087), B6.129S2-*H2*$^{dlAb1-Ea}$/J (no. 003584), B6(Cg)-*Zbtb46*$^{tm1(HBEGF)Mnz}$/J (no. 019506), B6.129S1-*Il12b*^{tm1Jm}/J (no. 002693) mice were also purchased from JAX, *Ccl19*$^{-/-}$ mice were donated by J. G. Cyster and C57BL/6NF-*Wdfy4*$^{em1(IMPC)J}$/J (no. 029334 and MMRRC no. 051082-JAX) were donated by K. M. Murphy. All animal experiments performed in this study were approved by the Institutional Animal Care and Use Committee at the Icahn School of Medicine at Mount Sinai (IACUC no. LA10-00021 and no. 04-0274). Mice within experiments were age and sex-matched. Tumor implantations were conducted in mice between 7 and 15 weeks of age. Mice were housed in individually ventilated cages at the Mount Sinai specific pathogen–free (SPF) facilities, provided food and water ad libitum, with conditions maintained at 21° to 23°C and 39 to 50% humidity and 12 hour–12 hour dark-light cycle.

B6.129P2-*Trp53*^{tm1Brn}/J (p53LoxP, Trp53fl/fl) and B6.129S4-*Kras*^{tm4Tyj}/J(KrasLSL-G12D) were obtained from JAX (no. 008462 and no. 008179, respectively) and crossed to generate the KP GEMM inducible mouse line (*Kras*$^{LSL-G12D/+}$; *Trp53*$^{fl/fl}$). KP-GEMM-*Xcr1*-Venus strain was established by crossing the KP GEMM with *Xcr1*-Venus mice (*57*) (provided by W. Kastenmüller, University of Würzburg, Germany). KP-GEMM-*Batf3*$^{-/-}$ were generated by crossing the KP GEMM and the *Batf3*$^{-/-}$ mice (donated by C. Lehmann, Erlangen University hospital). Experiments with KP-GEMM lines were performed at the International Centre for Genetic Engineering and Biotechnology, ICGEB, Trieste, Italy by Benvenuti laboratory.

Bone marrow transplantation

Bone marrow (BM) chimeras were generated by retro-orbitally injecting 1 to 10 × 10^6 total donor cells (fresh or cryopreserved BM) into sub-lethally irradiated 6-week-old recipient mice (two doses of 5.5 Gy administered 6 hours apart). A period of 9 to 12 weeks was granted to ensure engraftment.

Recipients were supplemented with sulfamethoxazole/trimethoprim for 3 weeks. At 9 weeks, successful reconstitution (minimum 90%) was assessed by flow cytometry analysis of peripheral blood.

Generation of KP-HELLO-2 tumor model

KP-HELLO-2 cells were originally derived from the KP-HELLO cells (provided by N. S. Joshi) (*22*) and modified in house. MSCV-IRES-Thy1.1 DEST was a gift from A. Rao (Addgene cat. no. 17442), and gamma-retrovirus encoding Thy1.1 was produced by transfecting HEK 293T cells with Thy1.1 vector along with gamma retroviral packaging plasmids. Briefly, KP-HELLO cells were expanded on a tissue culture-coated plate. Upon reaching 60% confluence, they were transduced with retroviral particles by spinfection with polybrene (final concentration of 8 μg/ml). Cells were expanded in RPMI supplemented with 10% fetal bovine serum (FBS) and 1% Pen-strep, Glutamax and HEPES and Thy1.1$^+$ cells (stained with anti–Thy-1.1 PE-Cy7, clone: OX-7, BioLegend cat. no. 202518) were sorted twice over 10 passages on a CytoFLEX SRT Cell Sorter (Beckman).

Cell lines

KP-HELLO-2, KP-HELLO, and KPAR1.3 [provided by J. Downward (*58*)] cells were derived from a *Kras*$^{LSL-G12D/+}$;*p53*$^{fl/fl}$ background, AKPS colorectal tumor organoids from a *Apc*$^{fl/fl}$;*Kras*$^{LSL-G12D/+}$;*p53*$^{fl/fl}$;*Smad4*$^{fl/fl}$ background [provided by Ö. H. Yilmaz (*59*)], and Hep-53.4 HCC cells from a carcinogen-induced liver model [(*60*) Cellosaurus CVCL_5765] were provided by J. Llovet and originally obtained from Cytion (product no. 400200). All cell lines were grown in complete cell culture medium [Dulbecco's modified Eagle's medium (DMEM) + 10% FBS + 1% P/S].

Orthotopic tumor models

For orthotopic lung tumors, 1.5 × 10^5 KP-HELLO-2, KP-HELLO, or KPAR1.3 cells were intravenously injected into the tail vein. Tumor-bearing lungs and tumor-draining lymph nodes were analyzed 15 days postinjection, unless otherwise specified in the figure legends. For KPAR1.3, tumors were harvested 21 days postinjection. To assess tumor burden, the left lung lobe was fixed in paraformaldehyde (PFA), embedded in paraffin, and examined as 5 μm cross-sections. Upon hematoxylin and eosin (H&E) staining, lung tissue sections were scanned on slides using an Olympus digital scanner and analyzed using the Panoramic viewer and QuPath software. For orthotopic CRC tumors, mice received intra-ceacum injection of 1.5 × 10^5 AKPS cells in 10 μl basement-membrane extract (BME) (R&D Systems cat. no. 35-330-0502) and tumors were analyzed 6 weeks postinjection. For orthotopic HCC tumors, mice were injected orthotopically into the left-lateral lobe of the liver with 1 × 10^6 Hep53-4 cells in 10 μl phosphate-buffered saline (PBS) and tumors were harvested 2 weeks postinjection.

Autochthonous tumor induction

Lung tumors were initiated in KP-GEMM-*Xcr1*-Venus and KP-GEMM-*Batf3*$^{-/-}$ mice via intratracheal administration of 2.5 × 10^7 infectious particles of a replication-deficient adenoviral vector encoding Cre recombinase (Ad-CMV-iCre, Vector Biolab, cat. no. 1045). Mice were euthanized 5 to 8 weeks postinoculation, and tumor-bearing lungs were collected for analysis.

In vivo treatments

For prolonged and effective conditional depletion of cDCs or cDC1s, *Zbtb46-hDTR* and *Xcr1*$^{Cre/wt}$; *Rosa26*$^{DTR/wt}$ mice received an initial dose of DT (32 ng per g body weight, List Biological Laboratories cat. no. 150), followed by injections of 20 ng per g every 60 hours. To inhibit lymphoid cell egress from peripheral lymphoid organs, mice were administered 20 μg of FTY720 (Cayman Chemical, cat. no. 10006292) daily over the indicated time periods. To increase DC numbers, mice received 75 μg of FLT3L-Fc (Gilead) on day 8 after tumor engraftment. FLT3L (30 μg; Celldex, cat. no. CDX-301) was administered once daily for 9 consecutive days starting at day 7. To provide exogenous licensing signal to DCs, mice were treated with 100 μg of anti-CD40 agonist antibody (clone FGK4.5, BioXCell, cat. no. BE0016-2) on days 7 and 11 after tumor engraftment. To deplete CD4$^+$ T cells, mice received 500 μg

of anti-CD4 antibody (clone GK1.5, BioXCell, cat. no. BE0003-1) on days 5 and 10 after tumor engraftment. To deplete $CD8^+$ T cells, mice received 200 μg of anti-CD8β (clone Lyt 3.2, BioXCell, cat. no. BE0223) antibody on the same days. Control mice received the corresponding isotype control antibody at the same dose and schedule. To labeled GMP-derived cells, $Ms4a3^{CreERT2}$;$Rosa^{TdT}$ mice received 2.5 mg of tamoxifen dissolved in corn oil daily from day 10 to day 15 after tumor engraftment (Sigma-Aldrich, cat. no. T5648). To block cytokine secretion, mice were pretreated with 125 μg of Brefeldin A (Sigma-Aldrich, cat. no. B7651) for 12 hours (*61*). All treatments were administered intraperitoneally.

Adoptive cell transfer

In experiments analyzing tumor-specific CD4 T cells (SMARTA; $CD4^+$ T cells specific for the LCMV GP66–77 epitope) by imaging, $CD4^+$ T cells were isolated from blood of naïve SMARTA CD45.1 transgenic mice with the EasySep Mouse $CD4^+$ T Cell Isolation Kit (StemCell, cat. no. 19852). Between 20 and 50×10^3 naïve SMARTA $CD4^+$ T cells were transferred intravenously into C57BL/6 recipient mice 1 day before tumor injection.

Flow cytometry

Single-cell suspensions were obtained from tumor bearing lung and tumor draining lymph nodes by digestion with 0.25 mg/ml collagenase IV (Sigma, cat. no. C5138-1G) at 37°C for 30 min (lung) or 25 min (lymph nodes) followed by passing through a 70-μm cell strainer and red blood cell lysis (RBC lysis buffer, BioLegend, cat. no. 420301) for 2 min at room temperature (RT). For T cell cytokine assessment, cells were incubated with 1 μg/ml brefeldin A, 1 μg/ml ionomycin, and 50 ng/ml phorbol 12-myristate 13-acetate (PMA) (all from Sigma, cat. nos. B7651, I0634, P1585) for 4 hours at 37°C. Cells were stained in fluorescence-activated cell sorting (FACS) buffer [PBS supplemented with 10% bovine serum albumin (BSA) and 2 mM EDTA] for 25 min at 4°C. For CCR7 and CXCR5 staining, cells were incubated for 30 min at 37°C. To assess tumor-specific $CD4^+$ T cells, cells were stained at 37°C for 2 hours with an APC-conjugated MHC-II LCMV Gp66 tetramer (generated from I-Ab LCMV GP 66-77 DIYKGVYQFKSV Monomers produced by the NIH Tetramer Core Facility and provided by A. O. Kamphorst) used at a 1:100 dilution. Cytokines and transcription factors were stained after fixation and permeabilization using the Foxp3/Transcription Factor Staining Buffer Set (eBioscience, cat. no. 00-5523-00). Samples Cells were analyzed with BD LSR Fortessa or BD FACSymphony analyzers (BD Biosciences). Flow cytometry data were acquired using FACS Diva software v.9 (BD), and the data obtained were analyzed using FlowJo (LLC). Antibodies used are listed in table S3. Gating strategies are shown in table S6.

Tumor-specific antibody binding assay

To measure tumor-binding antibodies, serum was collected from tumor-bearing mice at end point and heat-inactivated at 56°C for 10 min. KP-HELLO-2 cells were stained with serum (1:50) for 40 min at 4°C followed by a secondary staining with anti-mouse IgG (1:200, Poly4053-PE-Cy7, Biolegend, cat. no. 405315) or anti-mouse IgM (1:200, II/41-PerCP-eFluor710, eBioscience, cat. no. 46-5790-82) for 40 min at 4°C.

Immune aggregate formation using KP-HELLO-2 spheroids cocultured with mutuDCs and TILs

KP-HELLO-2 spheroids were cultured for 7 days as previously described (*62*) with 10,000 KP-HELLO-2 cells expressing mScarlet per spheroid, using the Spherotribe kit (Idylle). In parallel, mutuDCs were cultured with KP-HELLO-2 cell debris to induce maturation which was confirmed by flow cytometry (*12*, *63*). Separately, TILs were harvested and sorted from KP-HELLO-2 tumors 7 days postinjection, maintaining the endogenous T cell/B cell ratio, and labeled with DeepRed cell tracker for 30 min. Mature mutuDCs were added to KP-HELLO-2 spheroids for 4 hours, followed by the addition of TILs (30,000 mutuDCs and 30,000 TILs per spheroid). After 5 days, KP-HELLO-2 spheroid size and subsequent immune attraction were assessed by microscopy and ImageJ. Spheroid infiltration by TILs and three-dimensional (3D) aggregate formation in the presence of mutuDCs were measured by BiPhoton microscopy and analyzed with QuPath. The total number of TILs in KP-HELLO-2 spheroids cocultured with mutuDCs was also measured by flow cytometry.

Immunofluorescence imaging for TLS assessment

The left lung lobe was fixed overnight in 4% PFA and subsequently stored in 70% ethanol until further processing. The lungs were sectioned into 5 μm thick slices from formalin-fixed paraffin-embedded (FFPE) tissue. 5 μm FFPE slides were baked at 60°C for 2 hours before deparaffinization. Slides were deparaffinized in xylene (two treatments) and rehydrated through a series of ethanol solutions of decreasing concentrations (from 100% to 70%), followed by PBS rinses. For antigen retrieval, slides were immersed in prewarmed DAKO pH 9 solution (with or without 10% glycerol) at 95°C, then allowed to cool to RT and washed in PBS. Blocking was performed in a humidified chamber with a blocking buffer (1× TBS, 10% BSA, 0.1% Triton X-100). Autofluorescence was quenched with TrueBlack solution, followed by a PBS wash. Slides were incubated with primary antibody (1:200) in blocking buffer overnight at 4°C. After PBS washes, slides were incubated with secondary antibody, diluted 1:500 in PBS and containing 2% serum from the host species, and counterstained with 4′,6-diamidino-2-phenylindole (DAPI). Finally, slides were mounted with ProLong Gold Antifade Mountant (Invitrogen, cat. no. P36930), coverslipped, and stored at 4°C. Whole stained slides were scanned on a CyteFinder HT II fluorescence scanner (RareCyte) equipped with a 20× lens. Images were corrected for optical distortion, stitched and processed locally using the on-board CyteHub software. Alternatively, whole-slide images were captured using a Leica DMi8 microscope. Antibodies used are listed in table S3.

Machine learning TLS detection using Qupath

To detect TLSs in the entire left lung lobe at a whole-slide level, Random Trees pixel classifiers were applied in QuPath (*64*) with a resolution setting of 5.20 μm/pixel, selecting three channels (Alexa 488, Alexa 647, and DAPI) at scales of 2.0 and 4.0, using Gaussian features without normalization. Classifiers were trained on at least five manually annotated TLS regions (aggregates of $B220^+$ cells, $CD3^+$ cells, and $DAPI^+$ cells) and five non-TLS regions. The output classifications were then segmented into individual annotations with areas exceeding 1500 μm^2. Immune aggregate classifications were reviewed and validated by a trained pathologist.

Tumor antigen–specific B and T cell imaging

Before immunofluorescence staining, 10 μm OCT slides were fixed in acetone at −20°C for 10 to 15 min and dried. To detect tumor antigen–specific B cells targeting hen egg lysozyme (HEL), HEL protein (Sigma, cat. no. 10837059001) was conjugated to Alexa Fluor 488 using the Alexa Fluor 488 Protein Labeling Kit (ThermoFisher) according to the 20 to 50 kDa protein protocol. OCT-embedded slides were stained with HEL-Alexa488 (1:500) and costained with B220, GL7, and DAPI. To detect tumor antigen–specific $CD4^+$ T cells recognizing the LCMV GP66–77 epitope, OCT-embedded slides from adoptively transferred SMARTA CD45.1 mice were stained with CD45.1 and costained with CD4, PD-1, and DAPI (table S3).

Multispectral imaging for TLS maturity assessment

For multispectral staining, every cycle of antigen staining was processed as follows. The tissues were subjected to HIER either in AR6 or AR9 citrate buffers (Akoya Biosciences). After antigen retrieval, slides were blocked with 1× antibody diluent/block (Akoya Biosciences) for 10 min, followed by staining with primary antibody for 30 min. Every staining step took place in a humidified chamber at RT. After the wash with 1× TBS-Tween (TBST) buffer (3 times 2 min each), the slides were stained with HRP-conjugated secondary antibody, either anti-rabbit IgG

(Fisher, cat. no. MP740150) or anti-Rat IgG (Biocare, cat. no. RT517L) for 30 min. Then after the wash with 1× TBST, separate opal detector fluorophores were used for each marker. TLS maturity panel was as follows: CD4 (1:200)/Opal 480, CD8 (1:400)/Opal 780, CD19 (1:1000)/Opal 520, Ki67 (Clone SP6, ThermoFisher, 1:100, cat. no. MA5-14520)/Opal 570, CD21 (Clone SP186, Abcam, 1:50, cat. no. ab227662)/Opal 620, and AID (Clone mAID-2, ThermoFisher, 1:800, cat. no. 14-5959-82)/Opal 690. The last round of staining was carried out with additional antigen retrieval and DAPI nuclear staining. The staining was performed either manually or on automated machine (Opal 6-Plex Detection Kit, Akoya Biosciences, cat. no. NEL871001KT). Then the stained tissue sections were mounted with Diamond Anti-fade mounting media and were imaged as whole slides scans on the Vectra (Perkin Elmer). Images were unmixed and were analyzed on QuPath.

QuPath tissue analysis for TLS maturity assessment

QuPath software was used for quantification analysis. Cell detection and segmentation was carried out using StarDist extension based on DAPI nuclear stains (*65*) For phenotyping of individual cells, machine learning approach was used to generate an object classifier for each marker. In the case of markers that are mutually exclusive, we generated a group object classifier that includes all those markers. Then, these individual classifiers were compiled together and applied onto multispectral images to phenotype cells. For annotations of TLS, machine learning approach was once again used to generate a pixel classification with the annotation size greater than 1500 μm^2 (*66*, *67*).

Cyclic immunofluorescence (CyCIF)

Staining and imaging: FFPE sections were prepared and stained using a 20-plex antibody panel following previously described CyCIF methodologies. For sample preparation, slides were automatically baked at 60°C for 30 min and dewaxed at 72°C using BOND Dewax Solution. Antigen retrieval was carried out at 100°C for 20 min in BOND Epitope Retrieval Solution 2 (ER2) using a Leica Bond RX system. To minimize autofluorescence, slides were treated with a bleaching solution (4.5% H_2O_2, 20 mM NaOH in PBS) and exposed to light-emitting diode (LED) light for 2 cycles of 45 min. To reduce nonspecific antibody interactions, slides were rinsed in PBS for 3 × 5 min and incubated overnight at 4°C with secondary antibodies diluted 1:1000 in 150 µl of Odyssey Blocking Buffer, protected from light. Slides were then washed three times with PBS and bleached again for 2 × 45 min. For each round of CyCIF, samples were incubated overnight at 4°C in the dark with Hoechst 33342 (1:10,000; Thermo Fisher Scientific, cat. no. H3570) for nuclear staining, alongside either primary conjugated antibodies or primary unconjugated antibodies diluted as specified (table S3) in 150 µl of Odyssey Blocking Buffer (LI-Cor). When using primary unconjugated antibodies, incubation was followed by a 2-hour RT incubation with secondary antibodies in the dark. Subsequently, slides were washed 3 × 5 min and mounted with 200 µl of 70% glycerol. Imaging was performed automatically on a RareCyte Cytefinder II HT system, with exposure settings optimized per channel to prevent signal saturation while remaining consistent across samples. After imaging, coverslips were removed by placing slides in 1× PBS and heating them in a water bath for 1 hour. Between cycles, slides were photobleached for 2 × 45 min and washed 3 × 5 min in PBS (*68*–*70*).

Image preprocessing and quality control: The entire preanalytical CyCIF image processing workflow, including stitching, registration, illumination correction, segmentation, and single-cell feature extraction, was carried out using the MCMICRO pipeline, an open-source multiple-choice microscopy platform (full code available at GitHub: https://github.com/labsyspharm/mcmicro). For probability map generation, a pretrained U-Net model, UnMicst v2, was applied, followed by a marker-controlled watershed algorithm for single-cell segmentation. Nuclear detection was performed within a diameter range of 3 to 60 pixels. Probability maps generated by UnMicst were subsequently processed with S3segmenter to produce nuclear segmentation masks, and the cytoplasmic regions were defined by expanding the nuclear mask by 3 pixels. After segmentation masks were created, mean fluorescence intensities for each marker were computed for each cell, resulting in a single-cell data table corresponding to each acquired whole-slide CyCIF image. Annotated histologic regions on the whole-slide image were used to extract quantified single-cell data for cells located within the specified ROI range (TLS were identified by CD4, CD8, PD-1, B220, and DAPI staining using QuPath). Multiple strategies were used to ensure the accuracy and reliability of the single-cell data. At the image level, cross-cycle image registration and tissue integrity were reviewed, and poorly registered regions or areas with deformed tissues or artifacts were identified and excluded from the analysis. Antibodies exhibiting low-confidence staining patterns, as determined through visual inspection, were also removed from the analysis. Segmentation quality was rigorously assessed, and segmentation parameters were refined iteratively to enhance the precision of the segmentation masks. At the single-cell data level, correlations of DNA staining intensities across different cycles were evaluated to filter out cells lost during the cyclic process, using a correlation coefficient threshold of less than 0.8 for exclusion (*71*).

Single-cell phenotyping: To perform phenotype-driven gating, we used the open-source software Gater (https://github.com/labsyspharm/minerva_analysis), which allows definition of gating thresholds, cutoff values used to separate marker-positive from marker-negative cells. This gating process was independently applied to each individual image.

In summary, cells were assigned to specific phenotype categories based on the presence or absence of marker expression, as defined in a relational logic table (see CyCIF gating strategy, table S5). Cells that did not satisfy any of the Boolean logic rules defined in the phenotyping worksheet were labeled as "unknown." The logical operators AND, OR, ANY, and ALL were used in conjunction with POS (positive) and NEG (negative) expression criteria to characterize cell types identified through unsupervised clustering and manual review of tissue images. Once cell identities were determined, we validated these annotations by superimposing phenotype labels onto the original images using Napari via the image_viewer function embedded in scimap (https://napari.org/stable/).

Neighborhood analysis: Spatial neighborhoods were defined by calculating the Euclidean distance between cell centroids. For each reference cell type, neighboring cells within a 30 µm radius were identified. Interaction tables were generated recording each reference-neighbor cell pair, their cell types, and distance. Interactions were summarized as absolute counts and relative fractions per reference cell. TLS association was assigned by spatial overlap with TLS polygons (TLS were identified by CD4, CD8, PD-1, B220, and DAPI staining using QuPath), allowing comparisons of interactions within TLS versus non-TLS regions.

Multiplex immunohistochemistry (IHC) imaging

FFPE sections (4 µm) were stained using the multiplexed immunohistochemical consecutive staining on a single slide (MICSSS) protocol as previously described (*72*). Briefly, slides were baked at 50°C overnight, deparaffinized in xylene and rehydrated in decreasing concentration of ethanol (100%, 90%, 70%, 50% and dH_2O). Sample slides were incubated in pH6 or pH9 buffers at 95°C for 30 min for antigen retrieval, then in 3% hydrogen peroxide for 15 min and in serum-free protein block solution (Dako, cat. no. X090930-2) for 30 min. Primary antibody staining was performed using the optimized dilution during 1 hour at RT or at 4°C overnight followed by signal amplification using associated secondary antibody conjugated to horseradish peroxidase during 30 min. Chromogenic revelation was performed using AEC (Vector, cat. no. SK-4200). Tissue sections were counterstained with hematoxylin, mounted with a glycerol-based mounting medium and

finally scanned to obtain digital images (Aperio AT2, Leica). After scanning, slide coverslips were removed in hot water (~50°C). Primary antibodies are presented in table S3.

To quantitatively analyze localization and coexpression patterns, tissue annotation was first done by pathologists using QuPath software. For the analysis, we used the svs multiresolution, pyramidal images obtained per marker after staining. Both the AEC chromogen stain and the hematoxylin nuclear counterstain were extracted from each image via a dynamically determined deconvolution matrix. Then, each image was split into smaller tiles to permit computational analysis. Each tile from the first stained image was matched to the respective tile from the sequential stained images and then elastically registered using the extracted hematoxylin nuclear stain and SimpleElastix open-source software. Then, by using an iterative nuclear masking via STARDIST, we produced a composite semantic segmentation for nuclei residing in the series of tiles. Each nucleus was artificially expanded by a number of pixels to simulate a cytoplasm per cell and that was coherent with membrane marker staining. Finally, cellular-resolution metadata was acquired for all cells in the final cell mask. To unbiasedly determine positive and negative cells per marker, we used an unsupervised classification technique to cluster cell populations, followed by a supervised approach where we would evaluate each cluster as positive or negative per marker. First, the metadata aggregated per sample was collected, transformed to z-scores, randomized, and split into subsamples per batch. Each batch was processed in parallel: data for each marker were transformed, clustered and collapsed into multiple groups by principal components analysis (PCA) and uniform manifold approximation and projection (UMAP). Then, we performed the final quality control to manually attribute which clusters were positive or negative. This produced a final cellular-resolution data frame containing binary marker classification that was used for downstream localization, marker coexpression, tissue annotation and reconciliation and statistical analyses (*73*).

TLS 3D imaging using Lightsheet

Mice were euthanized by CO_2 and perfused transcardially with 10 ml 1× PBS. The post-caval lobe was collected from each mouse and placed in 4% PFA overnight at 4°C. Lungs were then prepared with LifeCanvas epoxy-based fixatives: samples were shaken for 1 day in fresh 50% SHIELD Epoxy/25% SHIELD buffer/25% water, then overnight in 7:1 SHIELD ON/SHIED Epoxy at 4°C. Subsequently, samples were moved to 100% SHIELD ON at 37°C for 2 days. Next, samples were passively delipidated by shaking at 37°C in LifeCanvas Delipidation Buffer for 11 days. Samples were permeabilized in blocking buffer—PBSTN (1% TritonX, 0.02% Sodium Azide, 1× PBS) with 5% donkey serum—at 37°C for 2 days, and then incubated in primary antibody (1:200) in blocking buffer for 4 days at 37°C. Samples were washed in PBSTN for 6 hours at 37°C and fixed overnight in 4% PFA at RT. After 4 hours of PBSTN washes, samples were incubated in secondary antibodies (1:500) in blocking buffer for 4 days at 37°C. As with the primary antibody, samples were washed in PBSTN for 6 hours, fixed in 4% PFA overnight, and washed again in PBSTN for 4 hours. To clear the samples, they were moved to 50% LifeCanvas EasyIndex (Refractive Index 1.52)/50% water overnight at 37°C, then to 100% LifeCanvas EasyIndex overnight at RT. Samples were mounted in low melting point agarose in 100% EasyIndex before imaging with the 9× objective in EasyIndex Matched Immersion Oil on the SmartSPIM light sheet microscope.

Experimental study design for in vivo studies

Sample size determination: No statistical method was used to predetermine sample size. Sample sizes were instead chosen based on field standards and previous experience with similar models. Sample sizes are consistent with those commonly used in in vivo tumor immunology experiments and were deemed sufficient to detect robust and biologically meaningful effects.

Randomization: Animals were randomly assigned to treatment or control groups to minimize bias when possible. This was achieved by alternating mice from different cages into different groups. No formal randomization software was used.

Blinding: Blinding was applied where possible. Investigators conducting histological quantification and flow cytometry gating were blinded to the treatment/genetic group during analysis.

Inclusion-exclusion criteria: Mice were included based on correct genotype, sexmatching, and absence of signs of illness or poor health at the time of tumor injection. No mice were excluded postrandomization unless they showed unrelated health issues or experimental error (e.g., tumor injection failure).

Human subjects

Samples of tumor were obtained from patients undergoing surgical resection at Mount Sinai Hospital (New York, NY) after obtaining informed consent in accordance with a protocol reviewed and approved by the Institutional Review Board at the Icahn School of Medicine at Mount Sinai (IRB Human Subjects Electronic Research Application 18-00407 for HCC samples, 10-00472 and 10-00135 for NSCLC samples and 18-00407 and 18-00855 for CRC samples) and in collaboration with the Biorepository and Department of Pathology. For multiplex imaging of patient TLS maturity conducted at the University of Pittsburgh, Pittsburgh, PA, the studies were performed under IRB protocols STUDY19060269 (NSCLC patients) and PRO17080326 (HGSOC patients).

The single-arm, open-label, phase 2 trial of HCC patients with resectable tumors was registered on ClinicalTrials.gov (NCT03916627, Cohort B). Twenty patients were enrolled and received two cycles of Cemiplimab before surgical resection as described in (*20*). Response to treatment was defined as more than 50% (partial response) or more than 70% (complete response) necrosis of resected tumor by pathologists. Similarly, TLSHi versus TLSLo status was determined based on pathologist annotation and H&E scoring, with patients classified as TLSHi when three or more TLS were identified in the resected tissue, and TLSLo when zero to two TLS were observed.

Postoperatively, patients underwent standard-of-care screening every 6 months; recurrence was defined as development of imaging consistent with recurrent HCC using the Liver Imaging Reporting and Data Systems (LIRADS) score of 5 for an intrahepatic lesion (the most common site of HCC recurrence) or arterial enhancing new extrahepatic metastatic foci consistent with metastatic disease (*74*). Detailed clinical information for the NSCLC POPLAR cohort (*18*) and the ccRCC BIONIKK cohort (*19*) are provided in the corresponding publications.

Metastatic breast cancer (MBC) tissue is from a clinical trial of an in situ vaccine for lymphoma, breast cancer and head and neck cancer (NCT03789097, Marron *et al.*, SITC 2022). A patient with cutaneous involvement of her MBC was enrolled on a clinical trial of an in situ vaccine, composed of intratumoral daily injections of FLT3L for 2 weeks to recruit DCs to the tumor microenvironment and dLNs, followed by low-dose radiation to the injected lesion to release tumor antigen, and then intratumoral poly-ICLC, the TLR3 ligand, to activate cDC1s. Patients underwent biopsies before and after FLT3L administration to assess effect on the tumor microenvironment.

The patient clinical metadata can be found in table S1.

10x Visium SD spatial transcriptomics

10x Visium spatial sequencing library preparation: Before processing Visium gene expression samples, DV200 was measured on RNA isolated from FFPE blocks to assess RNA integrity. Samples with a DV200 greater than 50% were selected for subsequent steps. After quality control, blocks were trimmed and 5-μm tissue sections were cut and placed on the capture area of a Visium Spatial Gene Expression for FFPE slide (10x Genomics). The slide was incubated in a thermal cycler

at 42°C for 3 hours and then placed in a desiccator overnight at RT. Subsequent steps covering tissue staining and library preparation were performed according to the manufacturer's instructions (CG000407_VisiumSpatialGeneExpressionforFFPE_RevC). The quality of the libraries was assessed using an Agilent 4200 TapeStation. Libraries were sequenced using the NovaSeq 6000 platform with 150 paired-end configuration on a NovaSeq SP flowcell.

Tested Visium FFPE samples with immune aggregates: The tested samples included in-house generated data for lung ($n = 3$), liver ($n = 3$) and colorectal ($n = 6$) human cancers and third-party dataset for renal ($n = 6$; GSE175540) human cancer. All the tested samples were stained using H&E. Visium transcriptome data were obtained using standard procedure provided by 10x Genomics for FFPE tissue sections. Reads were processed and mapped to the human reference genome *GRCh38* using the 10x Genomics Space Ranger pipeline (10x Genomics). Filtering and analysis of the samples were performed in python using scanpy (v1.9.1), with default parameters. In the downstream analysis, samples retained for further study were those containing at least one TLS per tissue area, as confirmed by a pathologist.

Deconvolution of Visium spots for spatial cell type mapping: For the deconvolution step we used Cell2location algorithm (*75*) yielding proportions of the deconvoluted cells in each Visium spot. We also performed H&E-based cell segmentation to quantify the number of cells per each Visium spot using StarDist (*65*). Then, we multiplied deconvoluted proportions of cells by the absolute number of segmented cells in each spot, thus getting the absolute number of deconvoluted cells in each Visium spot.

Spatial enrichment in TLS regions: For each Visium sample, we used the histopathological annotations of TLS as base to test the enrichment or depletion of inferred cell types. First, the inferred cell type abundance values are binarized based on their spatial autocorrelation using *Voyager* https://pachterlab.github.io/voyager/index.html (*76*). Univariate local statistics are calculated with the *runUnivariate* function (Getis-Ord GI* with permutation testing; type = "localG_perm") and spots were called if value > 2. Enrichment fold changes and statistics were calculated using *LotOfCells* (*77*). Correlation and hierarchical trees were calculated by *cor* and *hclust* functions. Visualizations were generated in R.

Gradient analysis: Gradient analysis consists of two steps. First, it identifies Visium spots positioned equidistantly from a selected structural boundary, whether they are inside the structure (internal layers) or moving away from it (outer layers). Then, it regresses gene expression or cellular counts across these layers and thus can explore the microenvironment of a selected tissue region (*78*).

Radial distance analysis from TLS regions: For each Visium sample, we used the TLS annotations to extract the radial distances, *d*, using the *RadialDistance* function in *semla* (convert_to_microns = T; v1.1.6; cit) (*79*). Distances of 0 μm represent the outer line of spots immediately exterior to the TLS-labeled spots. Distances >1000 μm were discarded to exclude distant tissue areas. In *ggplot2*, *geom_smooth* with the locally estimated scatterplot smoothing method ("loess," span = 0.45) was used for visualization of cell density data.

Pathway enrichment analysis of Visium samples: We used GSEApy (*80*) implementation of gene set enrichment analysis. Used databases of pathways: GO Cellular Component (https://geneontology.org/), KEGG (https://www.genome.jp/kegg/), LINCS (https://lincsproject.org/), MSigDB (https://www.gsea-msigdb.org/gsea/msigdb), and Reactome (https://reactome.org/).

Code sharing statement for analysis of Visium samples: All the code used for cell segmentation in Visium samples is available at the Human Immune Monitoring Center (HIMC) GitHub page https://github.com/ismms-himc/visium_segmentation. The code for gradient analysis is deposited in the HIMC GitHub page, https://github.com/ismms-himc/Visium_analysis.

Other packages used for Visium analysis: Seurat (*81*), Simple features (*82*), Tidyverse (*83*), Scran (*84*), and Scater (*85*).

10x Visium HD spatial transcriptomics

Nuclear segmentation and neighborhood analysis: Space Ranger outputs of Human lung Visium HD datasets were obtained from 10x Genomics website. Full-resolution tissue images (TIFF) were read alongside the corresponding 2 mm spatial transcriptomics outputs for each sample and processed with *sopa* (*86*) and *spatialdata* (*87*) packages. Nuclei segmentation was performed using the *stardist* (*88*) algorithm, with the FFPEIF_Experiment1 sample processed using the 2D versatile fluorescence model and all other samples using the default 2D versatile HE model (probability threshold 0.2, non-maximum suppression 0.6, minimum area 30). Segmented cell boundaries were exported as *GeoPackage* files, and per-cell features were aggregated with a radius expansion of one cell diameter. Gene expression tables were filtered to retain genes expressed in ≥10 cells and cells with ≥3 counts, normalized and log-transformed using *scanpy* (*89*). All processed data, including segmented images, polygon files, and AnnData objects (*90*), were saved for downstream analyses and visualization in R. Cell type annotations were assigned by implementing a K-Nearest Neighbors (KNN) classification approach using the *RunKNNPredict* function from *scop* package in R (https://github.com/mengxu98/scop) using combined human reference model of GSE154826, GSE206325, GSE183219 and of human CRC dataset (unpuplished). Spatial neighborhoods were defined by calculating the Euclidean distance between cell centroids. For each reference cell type, neighboring cells within a 30 μm radius were identified. Interaction tables were generated recording each reference-neighbor cell pair, their cell types, and distance. Interactions were summarized as absolute counts and relative fractions per reference cell (*82*). TLS association was assigned by spatial overlap with TLS polygons (previously identified using QuPath), allowing comparisons of interactions within TLS versus non-TLS regions.

scRNA-seq and single-cell T cell receptor sequencing (scTCR-seq) analyses

Previously published NSCLC and HCC scRNA-seq datasets (GSE154826, GSE206325) were analyzed. Differentially expressed genes were determined using Seurat. Imputed mean UMI counts were used to calculate logarithmic fold changes in expression between cell states to further analyze markers of interest. Gene set enrichment analysis was conducted using the Enrichr database. Additional R packages used include scDissector v1.0.0, shiny v1.7.0, ShinyTree v0.2.7, heatmaply v1.3.0, plotly v4.10.0, ggvis v0.4.7, ggplot2 v3.3.5, dplyr v1.0.7, Matrix v0.9.8, and seriation v1.3.5. The preprocessed raw count matrices were normalized and log1p-transformed before scoring for mature DC signature with sc.tl.score_genes() in Scanpy (*89*, *90*). Patients with <10 cells per cluster were removed from subsequent analysis. Additional Python libraries used include: Scanpy v1.9.8, anndata v0.10.5.post1, umapv0.5.5, numpyv1.26.4, scipy v1.12.0, pandas v2.2.3, scikit-learn v1.4.0, statsmodels v0.14.1, igraphv0.11.3, pynndescent v0.5.11. scTCR-seq was performed as described previously (*15*).

MERFISH

To identify transcriptionally distinct cell population with MERFISH, we used two panels of genes as previously described (*15*) (table S2). FFPE or fresh frozen samples from HCC and NSCLC patients were

processed as previously described and tissue sections were incubated with a custom designed MERSCOPE Gene Panel Mix for 36 to 48 hours at 37°C. Samples were gel embedded and underwent tissue clearing as previously described. Tissue slides were prepared for imaging as previously described and loaded onto the MERSCOPE system (Vizgen 10000001). Samples were initially imaged at low-resolution using 10× magnification to select regions of interest which were imaged at high-resolution using 60× magnification.

Images were visualized using MERSCOPE Vizualizer (v2.1.2593.1) and single-cell analysis was conducted using the the scanpy (v1.9.1) Python package as previously described. Briefly, cells with <10 and >750 counts or with <10 unique genes expressed were removed. Furthermore, cells with a high fraction of blank counts (top 5th percentile) or with high or low spot density or polyT signaling staining intensity (top and bottom 0.0005 percentile) were filtered to remove debris, apoptotic cells, and suspected doublets. Label transfer was performed using TACCO (v0.2.2) from annotated single-cell data to the MERFISH data using the MERFISH raw counts as inputs and default parameters for label transfer. For HCC samples, a previously published single-cell reference was used (*15*). For NSCLC samples, a mixture of the liver tumor single-cell reference and a prior lung adenocarcinoma atlas (*14*) was used due to the increased resolution of desired immune cell subtypes in the liver data. Specifically, clusters labeled as T, NK, DC, B memory, and B naïve from the HCC dataset replaced respective cell types in the NSCLC dataset. Resulting labels were compared against scanpy-based Leiden clustering of MERFISH data for concordance of broad cell type compartments. After label transfer, tissue regions were drawn using Shapely (v2.0.1) and GeoPandas (v0.14.0) around cells labeled naïve B and memory B cells, which were annotated as "immune aggregates." In HCC samples, regions were drawn around tumor, endothelial, and hepatic stellate cells, which were annotated as "stromal." In NSCLC sections, similar "stromal" regions were created around epithelial, endothelial, and fibroblast cell types. Regions were drawn as alpha shapes around cells, using the centroid x and y locations of each cell as inputs. To smooth regions of sparse cells, all regions were buffered by 30 μm. Overlapping areas of regions were resolved such that immune aggregate regions were prioritized first before stromal. Co-occurrence analysis was performed separately for cells of interest in stromal and immune aggregate regions using squidpy (v1.5.0) (*91*) using the squidpy.gr.co_occurrence() function at regular intervals from 0 to 500 μm and the TACCO assigned cell type labels as inputs. Enrichment values for each cell type at 30 μm were normalized for visualization by $\ln(1 + x)$, where x is the co-occurrence enrichment value as derived from squidpy. Co-occurrence results were also checked for agreement with permutation-based neighborhood enrichment, calculated through the squidpy.gr.nhood_enrichment() function. Gene module scores were calculated using sc.tl.score_genes() in a similar fashion to scRNA-seq scores. All MERFISH downstream processing and analysis was conducted on a distributed high performance computer cluster. This work was supported in part through the computational resources and staff expertise provided by Scientific Computing at the Icahn School of Medicine at Mount Sinai and supported by the Clinical and Translational Science Awards (CTSA) grant UL1TR004419 from the National Center for Advancing Translational Sciences.

POPLAR cohort

Survival analysis: Overall survival analyses of the POPLAR cohort (*18*, *92*, *93*) was performed using a Kaplan-Meier estimator and Cox regression upon stratifying patients by presence of TLS or lymphoid aggregates (LAs). TLS or LA annotations were determined by histological imaging. R packages used include: survival, survminer, and gtsummary.

Immune cell scores and pathway analyses: Gene signatures for different immune cell types were generated from prior literature (*14*, *15*) (table S4). Scores for each signature were computed as the mean of z-scores for each gene across patient samples. To determine correlations between immune cell scores, Pearson correlation coefficients were computed (two-tailed, 95% confidence interval). These signatures were also used to determine significant cell signaling pathways via gene set enrichment analysis (*94*).

Statistics

Parametric statistical tests, such as the two-tailed Student's *t* test (for unpaired comparisons) and paired *t* test (for paired comparisons), were used to assess differences between two groups when the data met normality assumptions. For nonparametric comparisons, normality was first evaluated using the Kolmogorov-Smirnov test (for unpaired data) or the Shapiro-Wilk test (for paired data). If the data significantly deviated from normality, a Mann-Whitney *U* test was used for unpaired comparisons, and a Wilcoxon signed-rank test was performed for paired samples. For comparisons involving more than two groups, one-way analysis of variance (ANOVA) followed by Tukey's multiple comparisons test was applied when normality assumptions were met. Kaplan-Meier curves were compared using the log-rank (Mantel-Cox) test.

REFERENCES AND NOTES

1. W. H. Fridman *et al.*, Tertiary lymphoid structures and B cells: An intratumoral immunity cycle. *Immunity* **56**, 2254–2269 (2023). doi: 10.1016/j.immuni.2023.08.009; pmid: 37699391
2. J.-L. Teillaud, A. Houel, M. Panouillot, C. Riffard, M.-C. Dieu-Nosjean, Tertiary lymphoid structures in anticancer immunity. *Nat. Rev. Cancer* **24**, 629–646 (2024). doi: 10.1038/s41568-024-00728-0; pmid: 39117919
3. R. Cabrita *et al.*, Tertiary lymphoid structures improve immunotherapy and survival in melanoma. *Nature* **577**, 561–565 (2020). doi: 10.1038/s41586-019-1914-8; pmid: 31942071
4. M.-C. Dieu-Nosjean *et al.*, Long-term survival for patients with non–small-cell lung cancer with intratumoral lymphoid structures. *J. Clin. Oncol.* **26**, 4410–4417 (2008). doi: 10.1200/JCO.2007.15.0284; pmid: 18802153
5. J. Goc *et al.*, Dendritic cells in tumor-associated tertiary lymphoid structures signal a Th1 cytotoxic immune contexture and license the positive prognostic value of infiltrating $CD8^+$ T cells. *Cancer Res.* **74**, 705–715 (2014). doi: 10.1158/0008-5472.CAN-13-1342; pmid: 24366885
6. B. A. Helmink *et al.*, B cells and tertiary lymphoid structures promote immunotherapy response. *Nature* **577**, 549–555 (2020). doi: 10.1038/s41586-019-1922-8; pmid: 31942075
7. F. Petitprez *et al.*, B cells are associated with survival and immunotherapy response in sarcoma. *Nature* **577**, 556–560 (2020). doi: 10.1038/s41586-019-1906-8; pmid: 31942077
8. T. N. Schumacher, D. S. Thommen, Tertiary lymphoid structures in cancer. *Science* **375**, eabf9419 (2022). doi: 10.1126/science.abf9419; pmid: 34990248
9. V. Durai, K. M. Murphy, Functions of Murine Dendritic Cells. *Immunity* **45**, 719–736 (2016). doi: 10.1016/j.immuni.2016.10.010; pmid: 27760337
10. M. Guilliams *et al.*, Dendritic cells, monocytes and macrophages: A unified nomenclature based on ontogeny. *Nat. Rev. Immunol.* **14**, 571–578 (2014). doi: 10.1038/nri3712; pmid: 25033907
11. B. Maier *et al.*, A conserved dendritic-cell regulatory program limits antitumour immunity. *Nature* **580**, 257–262 (2020). doi: 10.1038/s41586-020-2134-y; pmid: 32269339
12. M. Belabed *et al.*, Cholesterol mobilization regulates dendritic cell maturation and the immunogenic response to cancer. *Nat. Immunol.* **26**, 188–199 (2025). doi: 10.1038/s41590-024-02065-8; pmid: 39838105
13. M. Meylan *et al.*, Tertiary lymphoid structures generate and propagate anti-tumor antibody-producing plasma cells in renal cell cancer. *Immunity* **55**, 527–541.e5 (2022). doi: 10.1016/j.immuni.2022.02.001; pmid: 35231421
14. A. M. Leader *et al.*, Single-cell analysis of human non-small cell lung cancer lesions refines tumor classification and patient stratification. *Cancer Cell* **39**, 1594–1609.e12 (2021). doi: 10.1016/j.ccell.2021.10.009; pmid: 34767762
15. A. Magen *et al.*, Intratumoral dendritic cell–$CD4^+$ T helper cell niches enable $CD8^+$ T cell differentiation following PD-1 blockade in hepatocellular carcinoma. *Nat. Med.* **29**, 1389–1399 (2023). doi: 10.1038/s41591-023-02345-0; pmid: 37322116
16. J. A. Grout *et al.*, Spatial Positioning and Matrix Programs of Cancer-Associated Fibroblasts Promote T-cell Exclusion in Human Lung Tumors. *Cancer Discov.* **12**, 2606–2625 (2022). doi: 10.1158/2159-8290.CD-21-1714; pmid: 36027053
17. C. Moussion, J.-P. Girard, Dendritic cells control lymphocyte entry to lymph nodes through high endothelial venules. *Nature* **479**, 542–546 (2011). doi: 10.1038/nature10540; pmid: 22080953
18. N. S. Patil *et al.*, Intratumoral plasma cells predict outcomes to PD-L1 blockade in non-small cell lung cancer. *Cancer Cell* **40**, 289–300.e4 (2022). doi: 10.1016/j.ccell.2022.02.002; pmid: 35216676
19. Y.-A. Vano *et al.*, Nivolumab, nivolumab–ipilimumab, and VEGFR-tyrosine kinase inhibitors as first-line treatment for metastatic clear-cell renal cell carcinoma (BIONIKK): A biomarker-driven, open-label, non-comparative, randomised, phase 2 trial. *Lancet Oncol.* **23**, 612–624 (2022). doi: 10.1016/S1470-2045(22)00128-0; pmid: 35390339

20. T. U. Marron *et al.*, Neoadjuvant cemiplimab for resectable hepatocellular carcinoma: A single-arm, open-label, phase 2 trial. *Lancet Gastroenterol. Hepatol.* **7**, 219–229 (2022). doi: 10.1016/S2468-1253(21)00385-X; pmid: 35065058
21. M. Damo *et al.*, Inducible de novo expression of neoantigens in tumor cells and mice. *Nat. Biotechnol.* **39**, 64–73 (2021). doi: 10.1038/s41587-020-0613-1; pmid: 32719479
22. C. Cui *et al.*, Neoantigen-driven B cell and CD4 T follicular helper cell collaboration promotes anti-tumor CD8 T cell responses. *Cell* **184**, 6101–6118.e13 (2021). doi: 10.1016/j.cell.2021.11.007; pmid: 34852236
23. Z. Liu *et al.*, Fate Mapping via Ms4a3-Expression History Traces Monocyte-Derived Cells. *Cell* **178**, 1509–1525.e19 (2019). doi: 10.1016/j.cell.2019.08.009; pmid: 31491389
24. G. Dunsmore *et al.*, Timing and location dictate monocyte fate and their transition to tumor-associated macrophages. *Sci. Immunol.* **9**, eadk3981 (2024). doi: 10.1126/sciimmunol.adk3981; pmid: 39058763
25. S. T. Ferris *et al.*, cDC1 prime and are licensed by CD4$^+$ T cells to induce anti-tumour immunity. *Nature* **584**, 624–629 (2020). doi: 10.1038/s41586-020-2611-3; pmid: 32788723
26. R. Mattiuz *et al.*, Type 1 conventional dendritic cells and interferons are required for spontaneous CD4$^+$ and CD8$^+$ T-cell protective responses to breast cancer. *Clin. Transl. Immunology* **10**, e1305 (2021). doi: 10.1002/cti2.1305; pmid: 34277006
27. R. Mattiuz *et al.*, Novel Cre-Expressing Mouse Strains Permitting to Selectively Track and Edit Type 1 Conventional Dendritic Cells Facilitate Disentangling Their Complexity *in vivo*. *Front. Immunol.* **9**, 2805 (2018). doi: 10.3389/fimmu.2018.02805; pmid: 30564233
28. D. J. Theisen *et al.*, WDFY4 is required for cross-presentation in response to viral and tumor antigens. *Science* **362**, 694–699 (2018). doi: 10.1126/science.aat5030; pmid: 30409884
29. C. S. Garris *et al.*, Successful Anti-PD-1 Cancer Immunotherapy Requires T Cell-Dendritic Cell Crosstalk Involving the Cytokines IFN-γ and IL-12. *Immunity* **49**, 1148–1161.e7 (2018). doi: 10.1016/j.immuni.2018.09.024; pmid: 30552023
30. S. A. Luther, H. L. Tang, P. L. Hyman, A. G. Farr, J. G. Cyster, Coexpression of the chemokines ELC and SLC by T zone stromal cells and deletion of the ELC gene in the *plt/plt* mouse. *Proc. Natl. Acad. Sci. U.S.A.* **97**, 12694–12699 (2000). doi: 10.1073/pnas.97.23.12694; pmid: 11070085
31. L. Ohl *et al.*, CCR7 governs skin dendritic cell migration under inflammatory and steady-state conditions. *Immunity* **21**, 279–288 (2004). doi: 10.1016/j.immuni.2004.06.014; pmid: 15308107
32. M. Matloubian *et al.*, Lymphocyte egress from thymus and peripheral lymphoid organs is dependent on S1P receptor 1. *Nature* **427**, 355–360 (2004). doi: 10.1038/nature02284; pmid: 14737169
33. J. Loschko *et al.*, Inducible targeting of cDCs and their subsets *in vivo*. *J. Immunol. Methods* **434**, 32–38 (2016). doi: 10.1016/j.jim.2016.04.004; pmid: 27073171
34. S. Eickhoff *et al.*, Robust Anti-viral Immunity Requires Multiple Distinct T Cell-Dendritic Cell Interactions. *Cell* **162**, 1322–1337 (2015). doi: 10.1016/j.cell.2015.08.004; pmid: 26296422
35. J. L. Hor *et al.*, Spatiotemporally Distinct Interactions with Dendritic Cell Subsets Facilitates CD4$^+$ and CD8$^+$ T Cell Activation to Localized Viral Infection. *Immunity* **43**, 554–565 (2015). doi: 10.1016/j.immuni.2015.07.020; pmid: 26297566
36. J. C. Osorio *et al.*, Fc-optimized CD40 agonistic antibody elicits tertiary lymphoid structure formation and systemic antitumor immunity in metastatic cancer. *Cancer Cell* **43**, 1902–1916.e9 (2025). doi: 10.1016/j.ccell.2025.07.013; pmid: 40816292
37. N. S. Joshi *et al.*, Regulatory T Cells in Tumor-Associated Tertiary Lymphoid Structures Suppress Anti-tumor T Cell Responses. *Immunity* **43**, 579–590 (2015). doi: 10.1016/j.immuni.2015.08.006; pmid: 26341400
38. K. G. McDonald, J. S. McDonough, B. K. Dieckgraefe, R. D. Newberry, Dendritic cells produce CXCL13 and participate in the development of murine small intestine lymphoid tissues. *Am. J. Pathol.* **176**, 2367–2377 (2010). doi: 10.2353/ajpath.2010.090723; pmid: 20304952
39. C. H. GeurtsvanKessel *et al.*, Dendritic cells are crucial for maintenance of tertiary lymphoid structures in the lung of influenza virus–infected mice. *J. Exp. Med.* **206**, 2339–2349 (2009). doi: 10.1084/jem.20090410; pmid: 19808255
40. S. Halle *et al.*, Induced bronchus-associated lymphoid tissue serves as a general priming site for T cells and is maintained by dendritic cells. *J. Exp. Med.* **206**, 2593–2601 (2009). doi: 10.1084/jem.20091472; pmid: 19917776
41. S. S. Nair *et al.*, Prostate cancer *in situ* autovaccination with the intratumoral viral mimic poly-ICLC: Modulating the cold tumor microenvironment. *Med* **6**, 100879 (2025). doi: 10.1016/j.medj.2025.100879; pmid: 41173002
42. S. Dähling *et al.*, Type 1 conventional dendritic cells maintain and guide the differentiation of precursors of exhausted T cells in distinct cellular niches. *Immunity* **55**, 656–670.e8 (2022). doi: 10.1016/j.immuni.2022.03.006; pmid: 35366396
43. M. Chaib *et al.*, Macrophage-Dendritic Cell-T-Cell Tetrads Orchestrate Antitumor Immunity and Response to Checkpoint Blockade. bioRxiv 2025.12.24.696419 [Preprint] (2025). doi: 10.64898/2025.12.24.696419
44. E. Alspach *et al.*, MHC-II neoantigens shape tumour immunity and response to immunotherapy. *Nature* **574**, 696–701 (2019). doi: 10.1038/s41586-019-1671-8; pmid: 31645760
45. G. Espinosa-Carrasco *et al.*, Intratumoral immune triads are required for immunotherapy-mediated elimination of solid tumors. *Cancer Cell* **42**, 1202–1216.e8 (2024). doi: 10.1016/j.ccell.2024.05.025; pmid: 38906155
46. K. Schumann *et al.*, Immobilized chemokine fields and soluble chemokine gradients cooperatively shape migration patterns of dendritic cells. *Immunity* **32**, 703–713 (2010). doi: 10.1016/j.immuni.2010.04.017; pmid: 20471289
47. B. Zitti *et al.*, Positioning and reversible suppression of CCR7$^+$ dendritic cells in perivascular tumor niches shape cancer immunity. *Immunity* **59**, 161–176.e12 (2026). doi: 10.1016/j.immuni.2025.11.020; pmid: 41421339
48. L. Onder *et al.*, Fibroblastic reticular cells generate protective intratumoral T cell environments in lung cancer. *Cell* **188**, 430–446.e20 (2025). doi: 10.1016/j.cell.2024.10.042
49. Y. Zhang *et al.*, CCL19-producing fibroblasts promote tertiary lymphoid structure formation enhancing anti-tumor IgG response in colorectal cancer liver metastasis. *Cancer Cell* **42**, 1370–1385.e9 (2024). doi: 10.1016/j.ccell.2024.07.006; pmid: 39137726
50. J. Rangel-Moreno *et al.*, The development of inducible bronchus-associated lymphoid tissue depends on IL-17. *Nat. Immunol.* **12**, 639–646 (2011). doi: 10.1038/ni.2053; pmid: 21666689
51. H. Mitsui *et al.*, Combined use of laser capture microdissection and cDNA microarray analysis identifies locally expressed disease-related genes in focal regions of psoriasis vulgaris skin lesions. *J. Invest. Dermatol.* **132**, 1615–1626 (2012). doi: 10.1038/jid.2012.33; pmid: 22402443
52. P. Meiser *et al.*, A distinct stimulatory cDC1 subpopulation amplifies CD8$^+$ T cell responses in tumors for protective anti-cancer immunity. *Cancer Cell* **41**, 1498–1515.e10 (2023). doi: 10.1016/j.ccell.2023.06.008; pmid: 37451271
53. R. A. Chaurio *et al.*, TGF-β-mediated silencing of genomic organizer SATB1 promotes Tfh cell differentiation and formation of intra-tumoral tertiary lymphoid structures. *Immunity* **55**, 115–128.e9 (2022). doi: 10.1016/j.immuni.2021.12.007; pmid: 35021053
54. T. Imai *et al.*, Selective recruitment of CCR4-bearing Th2 cells toward antigen-presenting cells by the CC chemokines thymus and activation-regulated chemokine and macrophage-derived chemokine. *Int. Immunol.* **11**, 81–88 (1999). doi: 10.1093/intimm/11.1.81; pmid: 10050676
55. S. Hannedouche *et al.*, Oxysterols direct immune cell migration via EBI2. *Nature* **475**, 524–527 (2011). doi: 10.1038/nature10280; pmid: 21796212
56. S. J. Im *et al.*, Defining CD8$^+$ T cells that provide the proliferative burst after PD-1 therapy. *Nature* **537**, 417–421 (2016). doi: 10.1038/nature19330; pmid: 27501248
57. C. Yamazaki *et al.*, Critical roles of a dendritic cell subset expressing a chemokine receptor, XCR1. *J. Immunol.* **190**, 6071–6082 (2013). doi: 10.4049/jimmunol.1202798; pmid: 23670193
58. J. Boumelha *et al.*, An Immunogenic Model of KRAS-Mutant Lung Cancer Enables Evaluation of Targeted Therapy and Immunotherapy Combinations. *Cancer Res.* **82**, 3435–3448 (2022). doi: 10.1158/0008-5472.CAN-22-0325; pmid: 35930804
59. N. Goto *et al.*, SOX17 enables immune evasion of early colorectal adenomas and cancers. *Nature* **627**, 636–645 (2024). doi: 10.1038/s41586-024-07135-3; pmid: 38418875
60. S. Kress *et al.*, *p53* mutations are absent from carcinogen-induced mouse liver tumors but occur in cell lines established from these tumors. *Mol. Carcinog.* **6**, 148–158 (1992). doi: 10.1002/mc.2940060210; pmid: 1382443
61. M. Martínez-López, S. Iborra, R. Conde-Garrosa, D. Sancho, Batf3-dependent CD103$^+$ dendritic cells are major producers of IL-12 that drive local Th1 immunity against *Leishmania major* infection in mice. *Eur. J. Immunol.* **45**, 119–129 (2015). doi: 10.1002/eji.201444651; pmid: 25312824
62. L. Lugand *et al.*, Methods for Establishing a Renal Cell Carcinoma Tumor Spheroid Model With Immune Infiltration for Immunotherapeutic Studies. *Front. Oncol.* **12**, 898732 (2022). doi: 10.3389/fonc.2022.898732; pmid: 35965544
63. S. A. Fuertes Marraco *et al.*, Novel murine dendritic cell lines: A powerful auxiliary tool for dendritic cell research. *Front. Immunol.* **3**, 331 (2012). doi: 10.3389/fimmu.2012.00331; pmid: 23162549
64. P. Bankhead *et al.*, QuPath: Open source software for digital pathology image analysis. *Sci. Rep.* **7**, 16878 (2017). doi: 10.1038/s41598-017-17204-5; pmid: 29203879
65. U. Schmidt, M. Weigert, C. Broaddus, G. Myers, "Cell Detection with Star-Convex Polygons" in *Medical Image Computing and Computer Assisted Intervention – MICCAI 2018*, A. F. Frangi, J. A. Schnabel, C. Davatzikos, C. Alberola-López, G. Fichtinger, Eds. (Springer, 2018), pp. 265–273.
66. I. P. MacFawn *et al.*, The activity of tertiary lymphoid structures in high grade serous ovarian cancer is governed by site, stroma, and cellular interactions. *Cancer Cell* **42**, 1864–1881.e5 (2024). doi: 10.1016/j.ccell.2024.09.007; pmid: 39393357
67. A. T. Ruffin *et al.*, B cell signatures and tertiary lymphoid structures contribute to outcome in head and neck squamous cell carcinoma. *Nat. Commun.* **12**, 3349 (2021). doi: 10.1038/s41467-021-23355-x; pmid: 34099645
68. J.-R. Lin *et al.*, Multiplexed 3D atlas of state transitions and immune interaction in colorectal cancer. *Cell* **186**, 363–381.e19 (2023). doi: 10.1016/j.cell.2022.12.028; pmid: 36669472
69. J.-R. Lin *et al.*, Highly multiplexed immunofluorescence imaging of human tissues and tumors using t-CyCIF and conventional optical microscopes. *eLife* **7**, e31657 (2018). doi: 10.7554/eLife.31657; pmid: 29993362
70. G. Mollaoglu *et al.*, Ovarian cancer-derived IL-4 promotes immunotherapy resistance. *Cell* **187**, 7492–7510.e22 (2024). doi: 10.1016/j.cell.2024.10.006; pmid: 39481380
71. D. Schapiro *et al.*, MCMICRO: A scalable, modular image-processing pipeline for multiplexed tissue imaging. *Nat. Methods* **19**, 311–315 (2022). doi: 10.1038/s41592-021-01308-y; pmid: 34824477
72. R. Remark *et al.*, In-depth tissue profiling using multiplexed immunohistochemical consecutive staining on single slide. *Sci. Immunol.* **1**, aaf6925 (2016). doi: 10.1126/sciimmunol.aaf6925; pmid: 28783673
73. M. Buckup *et al.*, Multiparametric cellular and spatial organization in cancer tissue lesions with a streamlined pipeline. *Nat. Biomed. Eng.* **10**, 517–531 (2026). doi: 10.1038/s41551-025-01475-9; pmid: 40855123
74. D. G. Mitchell, J. Bruix, M. Sherman, C. B. Sirlin, LI-RADS (Liver Imaging Reporting and Data System): Summary, discussion, and consensus of the LI-RADS Management Working

Group and future directions. *Hepatology* **61**, 1056–1065 (2015). doi: 10.1038/s41587-021-01139-4; pmid: 35027729
75. V. Kleshchevnikov *et al.*, Cell2location maps fine-grained cell types in spatial transcriptomics. *Nat. Biotechnol.* **40**, 661–671 (2022). doi: 10.1038/s41587-021-01139-4; pmid: 35027729
76. L. Moses *et al.*, Voyager: Exploratory single-cell genomics data analysis with geospatial statistics. bioRxiv 2023.07.20.549945 [Preprint] (2023). doi: 10.1101/2023.07.20.549945
77. Ó. González-Velasco, LotOfCells: Data visualization and statistics of single cell metadata. bioRxiv 2024.05.23.595582 [Preprint] (2024). doi: 10.1101/2024.05.23.595582
78. E. Radkevich *et al.*, Informing biologically relevant signal from spatial transcriptomic data. bioRxiv 2024.09.09.610361 [Preprint] (2024). doi: 10.1101/2024.09.09.610361
79. L. Larsson, L. Franzén, P. L. Ståhl, J. Lundeberg, *Semla*: A versatile toolkit for spatially resolved transcriptomics analysis and visualization. *Bioinformatics* **39**, btad626 (2023). doi: 10.1093/bioinformatics/btad626; pmid: 37846051
80. Z. Fang, X. Liu, G. Peltz, GSEApy: A comprehensive package for performing gene set enrichment analysis in Python. *Bioinformatics* **39**, btac757 (2023). doi: 10.1093/bioinformatics/btac757; pmid: 36426870
81. Y. Hao *et al.*, Dictionary learning for integrative, multimodal and scalable single-cell analysis. *Nat. Biotechnol.* **42**, 293–304 (2024). doi: 10.1038/s41587-023-01767-y; pmid: 37231261
82. E. Pebesma, Simple Features for R: Standardized Support for Spatial Vector Data. *R J.* **10**, 439–446 (2018). doi: 10.32614/RJ-2018-009
83. H. Wickham *et al.*, Welcome to the Tidyverse. *J. Open Source Softw.* **4**, 1686 (2019). doi: 10.21105/joss.01686
84. A. T. L. Lun, D. J. McCarthy, J. C. Marioni, A step-by-step workflow for low-level analysis of single-cell RNA-seq data with Bioconductor [version 2; peer review: 3 approved, 2 approved with reservations]. *F1000Research* **5**, 2122 (2016). doi: 10.12688/f1000research.9501.2
85. D. J. McCarthy, K. R. Campbell, A. T. L. Lun, Q. F. Wills, Scater: Pre-processing, quality control, normalization and visualization of single-cell RNA-seq data in R. *Bioinformatics* **33**, 1179–1186 (2017). doi: 10.1093/bioinformatics/btw777; pmid: 28088763
86. Q. Blampey *et al.*, Sopa: A technology-invariant pipeline for analyses of image-based spatial omics. *Nat. Commun.* **15**, 4981 (2024). doi: 10.1038/s41467-024-48981-z; pmid: 38862483
87. L. Marconato *et al.*, SpatialData: An open and universal data framework for spatial omics. *Nat. Methods* **22**, 58–62 (2025). doi: 10.1038/s41592-024-02212-x; pmid: 38509327
88. M. Stevens *et al.*, StarDist Image Segmentation Improves Circulating Tumor Cell Detection. *Cancers* **14**, 2916 (2022). doi: 10.3390/cancers14122916; pmid: 35740582
89. F. A. Wolf, P. Angerer, F. J. Theis, SCANPY: Large-scale single-cell gene expression data analysis. *Genome Biol.* **19**, 15 (2018). doi: 10.1186/s13059-017-1382-0; pmid: 29409532
90. I. Virshup *et al.*, The scverse project provides a computational ecosystem for single-cell omics data analysis. *Nat. Biotechnol.* **41**, 604–606 (2023). doi: 10.1038/s41587-023-01733-8; pmid: 37037904
91. G. Palla *et al.*, Squidpy: A scalable framework for spatial omics analysis. *Nat. Methods* **19**, 171–178 (2022). doi: 10.1038/s41592-021-01358-2; pmid: 35102346
92. L. Fehrenbacher *et al.*, Atezolizumab versus docetaxel for patients with previously treated non-small-cell lung cancer (POPLAR): A multicentre, open-label, phase 2 randomised controlled trial. *Lancet* **387**, 1837–1846 (2016). doi: 10.1016/S0140-6736(16)00587-0; pmid: 26970723
93. J. Mazieres *et al.*, Atezolizumab Versus Docetaxel in Pretreated Patients With NSCLC: Final Results From the Randomized Phase 2 POPLAR and Phase 3 OAK Clinical Trials. *J. Thorac. Oncol.* **16**, 140–150 (2021). doi: 10.1016/j.jtho.2020.09.022; pmid: 33166718
94. Z. Xie *et al.*, Gene Set Knowledge Discovery with Enrichr. *Curr. Protoc.* **1**, e90 (2021). doi: 10.1002/cpz1.90; pmid: 33780170

ACKNOWLEDGMENTS

We thank members of the Merad, Kamphorst, and Brown laboratories at the Marc and Jennifer Lipschultz Precision Immunology Institute at Mount Sinai for insightful discussions and feedback. We thank the Mount Sinai Flow Cytometry Core, the Microscopy and Advanced Bioimaging CoRE, |the Human Immune Monitoring Center (HIMC), the Center for Comparative Medicine and Surgery for animal husbandry, and the Biorepository and Pathology CoRE Laboratory (notably A. Soto and S. El Naggar) at the Icahn School of Medicine at Mount Sinai for support. We thank the NIH Tetramer Core Facility (NIH contract 75N93020D00005 and RRID:SCR_026557) for providing I-Ab LCMV GP 66-77 DIYKGVYQFKSV monomer. We thank the patients and their families for participating in the clinical studies. We recognize the invaluable assistance of B. Y. Nabet (Genentech), M. Dalod, R. Akyol, E. Tomasello (Centre d'Immunologie de Marseille-Luminy), A. R. Sanchez-Paulete, J. A. Grout, M. Buckup, D. Feng, A. Lozano, C. M. Wilk, A. Saffon, N. Yatim, C. Azimi, L. Montégut, T. Chin, C. Noel, E. Katzin, C. Falcomatà, S. Balan, S. S. Nair (Icahn School of Medicine at Mount Sinai), Z. Yin (Yale University School of Medicine), A. V. Tumanov (UT Health San Antonio), and M. Meylan (Dana-Farber Cancer Institute). The summary figure was created with BioRender under academic license. This work was supported in part through the computational resources and staff expertise provided by Scientific Computing at the Icahn School of Medicine at Mount Sinai. We are grateful to Boehringer Ingelheim, Inc., for their sponsorship and support in providing resources for CRC sample collection. We acknowledge Vizgen, Inc., for their sponsorship and support for MERFISH data generation in this study. Genentech/Roche funded the POPLAR trial. **Funding:** R.Ma. was supported by the 2021 AACR-AstraZeneca Immuno-oncology Research Fellowship, grant no. 21-40-12-MATT, and with J.-C.L. by the FCT - Fundação para a Ciência e Tecnologia, I.P. (grant nos. 2023.15874.PEX and 2024.17879.PEX). J.B. was supported by the CRI 2025 Irvington Postdoctoral Fellowship (CRI12960). E.A. was supported by the Scholarship Programme for Visiting Research Scientists from the Bodossaki Foundation (grant no. 9755). B.Y.S. was supported by the National Institutes of Health (NIH) Medical Scientist Training (T32GM146636) and a National Cancer Institute predoctoral fellowship (F30CA301790). M.D.P. was supported by the American Federation for Aging Research (2021 Diana Jacobs Kalman Scholarship for Research in the Biology of Aging). S.H. was supported by the National Cancer Institute (K00CA223043 and K99CA293148). M.T. was supported by a European Research Council (ERC) CoG grant (artFibro, 101088596). A.L. was supported by NIH/NCI R37CA230636, NIH/NCI R01CA251155, and the Damon Runyon-Rachleff Innovator Award. S.K.-S. was supported by grants from the NIH (U24 CA224319, R01 DK1222853, U2C ES030859, DA055434, 1R01 HL166720-01A1, and U01OH012621) and funding from Caribou Biosciences, Inc. M.S. was supported by grants R21AI180874, R21AI176069, R01AI160706, and R01DK130425. S.Gn. was partially supported by NIH grants CA224319, DK124165, CA263705, and CA196521. A.O.K. and T.U.M. were supported in part by the Tisch Cancer Institute Cancer Center Support Grant (P30 CA196521). M.M. was partially supported by NIH grants CA257195, CA254104, and CA154947. **Author contributions:** R.Ma. and M.M. conceptualized and obtained funding for the project. R.Ma. and J.L.B. performed experiments with the help of J.B., E.A., P.H., A.V., M.D.P., C.H., L.L., M.B., E.H., R.Me., S.H., J.An, R.A.O., E.N., and G.M.P. L.H., B.Y.S., E.R., M.D.P., I.H.-V., D.D., J.-C.L., I.F., M.M.S., E.G.K., and V.R. performed the computational analysis. P.H. designed the MERFISH libraries. R.Ma. and M.D.P. designed the gene lists for bulk sequencing analysis. A.V., R.D., and J.B. modified the KP-HELLO cell line. R.Ma., E.A., P.H., A.V., H.M.K., L.T., R.A.K., C.H., L.L., F.R., M.E.K., I.P.M., G.I., S.O., A.Te., H.M., N.S., E.N., S.Go., A.M.R., A.Ta., and H.S. performed multiplex imaging experiments and analyses. F.R. and R.Ma. performed the light-sheet experiments. M.B., G.M., and R.Ma. did the spheroid experiments. R.Ma., P.H., L.T., and S.H. processed the human samples. C.H. coordinated the clinical and research teams and managed clinical specimens. S.O. and A.D.P. provided pathological expertise for tissue annotation. M.N., M.T., J.Ah., N.B., A.L., Z.C., S.K.-S., J.D.B., M.S., C.M., S.Gn., F.G., K.M.M., C.S.-F., W.H.F., B.D.B., T.U.M., F.B., J.G.C., H.S., T.C.B., N.S.J., and A.O.K. provided intellectual input, essential reagents, and datasets. M.M. supervised the study. R.Ma. wrote the original draft. R.Ma., J.B., and M.M. wrote, reviewed, and edited the manuscript. All authors provided feedback on the manuscript draft. **Competing interests:** M.M. serves on the scientific advisory board and holds stock from Dren Bio Inc., Owkin Inc., Larkspur Inc., and Myeloid therapeutics Inc.; serves on the scientific advisory board of OSE Inc.; and receives funding for contracted research from Regeneron Inc. and Boehringer Ingelheim Inc. T.C.B. is a consultant for Galvanize Therapeutics, Mestag Therapeutics, Tallac Therapeutics, Attivare Therapeutics, and Kalivir Therapeutics and serves on the scientific advisory board of Tabby Therapeutics. T.U.M. has served on advisory and/or data safety monitoring boards for Rockefeller University, Regeneron Pharmaceuticals, Abbvie, Bristol-Meyers Squibb, Boehringer Ingelheim, Atara, AstraZeneca, Genentech, Celldex, Chimeric, Glenmark, Simcere, Surface, G1 Therapeutics, NGMbio, DBV Technologies, Arcus, and Astellas and has research grants from Regeneron, Bristol-Myers Squibb, Merck, and Boehringer Ingelheim. The M.S. laboratory has received unrelated funding support in sponsored research agreements from Phio Pharmaceuticals, 7Hills Pharma, ArgenX NV, Ziphius, and Moderna. S.Gn. reports past consultancy or advisory roles for Merck and OncoMed and research funding from Regeneron Pharmaceuticals, Boehringer Ingelheim, Bristol Myers Squibb, Celgene, Genentech, EMD Serono, Pfizer and Takeda, unrelated to the current work. S.Gn. and M.M. are named coinventors on an issued patent (US20190120845A1) for multiplex IHC to characterize tumors and treatment responses. The technology is filed through Icahn School of Medicine at Mount Sinai (ISMMS) and is currently unlicensed. This technology was used to evaluate tissue in this study, and the results could affect the value of this technology. C.M. was a Genentech Inc. employee when this work was performed and owned company stocks. C.M. is an inventor on the patent US20230279067A1 held by Genentech, Inc., that covers "Ligand fusion proteins for FLT3 and methods of use." N.B. is an extramural member of the Parker Institute for Cancer Immunotherapy (PICI), holds stock options in BreakBio, serves as an advisor and/or board member and holds stock options in Genotwin and DC Prime, serves as an advisor and/or board member and holds equity in Cell BioEngines, holds stock in Barinthus, is a consultant for and has received grant support from Merck Research Laboratories, has received drug product from Oncovir, and serves on the scientific advisory board of Aikium (stock options) and Epitopea. I.P.M. is a paid consultant for Galvanize Therapeutics, Inc. The remaining authors declare no competing interests. **Data, code, and materials availability:** An interactive website for exploring TLS spatial data (Visium SD/HD, MERFISH, and CyCIF) is available at https://rstudio-connect.hpc.mssm.edu/mattiuz_science2026_tls_spatial_data/. No new software pipelines were used in the study beyond those described in the relevant Materials and methods sections and in (*78*). All data analysis scripts use existing methods and are provided in a GitHub repository provided with this paper (https://github.com/Merad-Lab/Mattiuz2026_Manuscript_Code/). Processed matrix files and metadata for the human cancer FFPE Visium SD dataset and human HCC and NSCLC MERFISH datasets generated in this study are available under accession nos. GSE322553 (https://www.ncbi.nlm.nih.gov/geo/query/acc.cgi?&acc=GSE322553) and GSE327192 (https://www.ncbi.nlm.nih.gov/geo/query/acc.cgi?&acc=GSE327192). Accession nos. for reanalyzed published datasets include the human renal cancer FFPE Visium SD dataset (GSE175540), external NSCLC bulk RNA-seq dataset (EGAS00001005013), and NSCLC and HCC scRNA-seq datasets (GSE154826, GSE206325, and GSE183219). Public 10x Genomics Visium HD NSCLC datasets are available at these links: lunghd_1, https://www.10xgenomics.com/datasets/visium-hd-cytassist-gene-expression-human-lung-cancer-post-xenium-expt; lunghd_2, https://www.10xgenomics.com/datasets/visium-hd-cytassist-gene-expression-human-lung-cancer-post-xenium-expt; lunghd_3, https://www.10xgenomics.com/datasets/visium-hd-cytassist-gene-expression-libraries-of-human-lung-cancer-if; and lunghd_4, https://www.10xgenomics.com/datasets/visium-hd-cytassist-gene-expression-human-lung-cancer-fixed-frozen. *Xcr1*-Venus mice are available from T. Kaisho under an MTA with Wakayama Medical University. KP-HELLO-2 cells can be obtained for research use under a material transfer agreement from R.Ma. and M.M. through the Icahn School of Medicine at Mount Sinai. Any additional information required to interpret data reported in this paper is available from the corresponding author M.M. on request.

SUPPLEMENTARY MATERIALS

science.org/doi/10.1126/science.ady1678
Figs. S1 to S7; Tables S1 to S6; MDAR Reproducibility Checklist; Movies S1 and S2
Submitted 15 April 2025; resubmitted 16 December 2025; accepted 8 May 2026
10.1126/science.ady1678

Dendritic cells control tertiary lymphoid structure development and maintenance in cancer

Raphaël Mattiuz, Jesse Boumelha, Emmanouil Aerakis, Jessica Le Berichel, Pauline Hamon, Laszlo Halasz, Abishek Vaidya, Brian Y. Soong, Emir Radkevich, Hye Mi Kim, Matthew D. Park, Romain Donne, Leanna Troncoso, Rachel A. Kaplan, Clotilde Hennequin, Isaias Hernández-Verdin, Lucía López, Frederika Rentzeperis, Darwin D'Souza, Medard Ernest Kaiza, Ian P. MacFawn, Meriem Belabed, Guillaume Mestrallet, Etienne Humblin, Raphaël Merand, Samarth Hegde, Jean-Christophe Lone, Giorgio Ioannou, Sinem Ozbey, Igor Figueiredo, Alexander Tepper, Hajer Merarda, Nadine Serhan, Maximilian M. Schaefer, Jinping An, Ray A. Ohara, Erika Nemeth, Simon Goldstein, Amanda M. Reid, Moataz Noureddine, Alexandra Tabachnikova, Giulia Maria Piperno, Maria Tsoumakidou, Jalal Ahmed, Alexandros D. Polydorides, Nina Bhardwaj, Amaia Lujambio, Zhihong Chen, Edgar Gonzalez Kozlova, Seunghee Kim-Schulze, Joshua D. Brody, Michael Schotsaert, Christine Moussion, Sacha Gnjatic, Vladimir Roudko, Florent Ginhoux, Kenneth M. Murphy, Catherine Sautès-Fridman, Wolf Herman Fridman, Brian D. Brown, Thomas U. Marron, Federica Benvenuti, Jason G. Cyster, Hélène Salmon, Tullia C. Bruno, Nikhil S. Joshi, Alice O. Kamphorst, and Miriam Merad

Science **393** (6808), eady1678. DOI: 10.1126/science.ady1678

Editor's summary

Tertiary lymphoid structures (TLSs) are immune cell formations that accumulate in nonlymphoid tissues. TLSs can develop at sites of chronic inflammation such as tumor tissue and have been associated with favorable responses to cancer immunotherapy. However, the mechanisms that govern the formation of TLSs remain unclear. Mattiuz *et al*. performed spatial profiling of human tumors and reported a key role for type 1 conventional dendritic cells (cDC1s) in the development of TLSs (see the Perspective by Decker). Early formation of TLSs relied on T cells primed by cDC1s in tumor-draining lymph nodes. By contrast, the persistence of TLSs required cDC1 accumulation within tumors and antigen presentation to CD4# and CD8# T lymphocytes to sustain B and T cell effector responses. These findings highlight cDC1s as key regulators of TLS function in cancer. —Priscilla N. Kelly